Title

Functional consequences of postnatal interventions in a mouse model of Fragile X syndrome

Authors

Rais, Maham

Lovelace, Jonathan W

Shuai, Xinghao S

et al.

Publication Date

2022

DOI

10.1016/j.nbd.2021.105577

Peer reviewed

Neurobiology of Disease 162 (2022) 105577

Contents lists available at ScienceDirect

Neurobiology of Disease

journal homepage: www.elsevier.com/locate/ynbdi

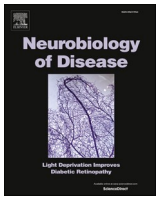

Functional consequences of postnatal interventions in a mouse model of Fragile X syndrome

Maham Rais [a], Jonathan W. Lovelace [b], Xinghao S. Shuai [a], Walker Woodard [a], Steven Bishay [a], Leo Estrada [a], Ashwin R. Sharma [a], Austin Nguy [a], Anna Kulinich [a], Patricia S. Pirbhoy [a], Arnold R. Palacios [a], David L. Nelson [d], Khaleel A. Razak [b,c], Iryna M. Ethell [a,c,*]

[a] Division of Biomedical Sciences and Biomedical Sciences Graduate Program, School of Medicine, University of California Riverside, Riverside, CA 92521, USA
[b] Department of Psychology, University of California Riverside, Riverside, CA 92521, USA
[c] Neuroscience Graduate Program, University of California Riverside, Riverside, CA 92521, USA
[d] Baylor College of Medicine, Houston, TX 77030, USA

ARTICLE INFO

Keywords:
Autism
Cortical deficits
Neurodevelopmental disorders
Parvalbumin inhibitory interneurons
Sensory processing disorders

ABSTRACT

Background: Fragile X syndrome (FXS) is a leading genetic cause of autism and intellectual disability with cortical hyperexcitability and sensory hypersensitivity attributed to loss and hypofunction of inhibitory parvalbumin-expressing (PV) cells. Our studies provide novel insights into the role of excitatory neurons in abnormal development of PV cells during a postnatal period of inhibitory circuit refinement.

Methods: To achieve *Fragile X mental retardation gene* (*Fmr1*) deletion and re-expression in excitatory neurons during the postnatal day (P)14-P21 period, we generated $Cre^{CaMKIIa}/Fmr1^{Flox/y}$ (cOFF) and $Cre^{CaMKIIa}/Fmr1^{FloxNeo/y}$ (cON) mice, respectively. Cortical phenotypes were evaluated in adult mice using biochemical, cellular, clinically relevant electroencephalogram (EEG) and behavioral tests.

Results: We found that similar to global *Fmr1* KO mice, the density of PV-expressing cells, their activation, and sound-evoked gamma synchronization were impaired in cOFF mice, but the phenotypes were improved in cON mice. cOFF mice also showed enhanced cortical gelatinase activity and baseline EEG gamma power, which were reduced in cON mice. In addition, TrkB phosphorylation and PV levels were lower in cOFF mice, which also showed increased locomotor activity and anxiety-like behaviors. Remarkably, when FMRP levels were restored in only excitatory neurons during the P14-P21 period, TrkB phosphorylation and mouse behaviors were also improved.

Conclusions: These results indicate that postnatal deletion or re-expression of FMRP in excitatory neurons is sufficient to elicit or ameliorate structural and functional cortical deficits, and abnormal behaviors in mice, informing future studies about appropriate treatment windows and providing fundamental insights into the cellular mechanisms of cortical circuit dysfunction in FXS.

1. Introduction

Fragile X Syndrome (FXS) is a common monogenic form of autism spectrum disorders (ASD) (Crawford et al., 2001). FXS is usually caused by a CGG repeat expansion in the 5′-untranslated region of the Fragile X mental retardation 1 (*Fmr1*) gene with consequent gene methylation, down-regulation of Fragile X Mental Retardation Protein (FMRP), translational dysregulation, and abnormal protein synthesis (Okray et al., 2015; Sutcliffe et al., 1992; Verkerk et al., 1991). Prominent symptoms of FXS include increased anxiety, intellectual disability, repetitive behaviors, social communication deficits, and abnormal sensory processing (Braat and Kooy, 2015; Penagarikano et al., 2007). Abnormal sensory processing in FXS includes debilitating hypersensitivity and reduced habituation to sensory inputs affecting multiple sensory systems, including the auditory domain (Castrén et al., 2003; Ethridge et al., 2016; Schneider et al., 2013). Emerging literature suggests early

Abbreviations: ASD, Autism spectrum disorders; AuC, Auditory Cortex; Fmr1, Fragile X mental retardation 1 gene; FMRP, Fragile X Mental Retardation Protein; FXS, Fragile X Syndrome; E/I, excitatory/inhibitory; MMP-9, matrix metalloproteinase-9; PNN, perineuronal nets; PV, parvalbumin.

* Corresponding author at: Division of Biomedical Sciences, USA.
E-mail address: iryna.ethell@medsch.ucr.edu (I.M. Ethell).

https://doi.org/10.1016/j.nbd.2021.105577
Received 3 July 2021; Received in revised form 22 October 2021; Accepted 2 December 2021
Available online 4 December 2021

sensory processing deficits may lead to broader autism-related phenotypes (Orefice et al., 2016).

Cortical hyperexcitability may cause auditory hypersensitivity in FXS, which is also observed in the mouse model of FXS (Castrén et al., 2003; Chen and Toth, 2001; Ethridge et al., 2016; Frankland et al., 2004; Nielsen et al., 2002; Rais et al., 2018; Rojas et al., 2001; Rotschafer and Razak, 2013; Rotschafer and Razak, 2014; Sinclair et al., 2017). The *fragile X mental retardation 1 gene* (*Fmr1)* knockout (KO) mouse is an established FXS model suited to study cortical deficits as it shows sensory hypersensitivity similar to humans with FXS. This similarity facilitates a circuit-level analysis of interactions between cortical excitation and inhibition that may cause hyperexcitability (Sinclair et al., 2017). However, the developmental role of FMRP in hyperexcitability and the cell types involved are still unclear.

Parvalbumin (PV) interneurons are fast-spiking inhibitory cells that provide temporal precision to excitatory responses, and their loss and hypofunction may contribute to cortical hyperexcitability in individuals with autism (Ferguson and Gao, 2018; Filice et al., 2020; Hashemi et al., 2017; Lunden et al., 2019; Marin, 2012; Rossignol, 2011) and mouse models of autism, including FXS (Goel et al., 2018). Our previous studies suggest that impaired development of PV inhibitory interneurons may underlie abnormal auditory cortical responses in *Fmr1* KO mice (Wen et al., 2018). FMRP loss reduces excitatory inputs on inhibitory interneurons (Gibson et al., 2008; Hays et al., 2011), and embryonic deletion of *Fmr1* in cortical excitatory neurons is sufficient to reduce PV expression, recapitulating abnormal electrophysiological and behavioral phenotypes that are seen in global *Fmr1* KO mice (Lovelace et al., 2020). However, it is still unclear whether the FMRP deletion affects PV cell neurogenesis, migration, or maturation. PV cells are derived from the precursor cells in the medial ganglionic eminence (MGE) (Lim et al., 2018). MGE-derived interneurons migrate to the cortex by birth and are already spontaneously active during the first postnatal week before expressing calcium-binding protein PV (del Rio et al., 1994; Kawaguchi et al., 1987). During the first postnatal week, PV cells also undergo apoptosis regulated by neuronal activity (Denaxa et al., 2018; Southwell et al., 2012; Wong et al., 2018). In the mouse cortex, PV cells start expressing PV and become fast-spiking interneurons during second and third postnatal weeks. PV cell maturation is influenced by sensory experience and restricts the activity of pyramidal cells leading to the closure of critical period plasticity (Hu et al., 2014; Marin, 2016). In addition, the maturation of PV interneurons is crucial for generating gamma rhythms (Cardin et al., 2009; Chen et al., 2017; Sohal et al., 2009; Guyon et al., 2021).

The main goal of this study was to examine whether deletion or re-expression of *Fmr1* during the critical developmental period of PV cell maturation (P14-P21) is sufficient to trigger or prevent the development of abnormal phenotypes in the auditory cortex (AuC) of *Fmr1* KO mice. We tested the hypothesis that cortical defects, in particular PV cell deficits and cortical responses, can be corrected by re-expressing FMRP only in excitatory neurons during the period of PV cell maturation, well after PV cells migrate to the cortex and undergo developmental death. Thus, the purpose of the present study is to understand the relationship between spatiotemporal aspects of FMRP expression and cortical hyperexcitability in FXS. These results will have broad implications in terms of prospects for gene reactivation studies by targeting specific cells and identifying optimal treatment windows.

2. Materials and methods

2.1. Ethics statement

All experiments and animal care/use protocols were approved by the Institutional Animal Care and Use Committee (IACUC) at the University of California, Riverside, and were carried out in accordance with the National Institute of Health (NIH) Guidelines for the Care and Use of Laboratory Animals.

2.2. Overview

The CaMKIIα promoter was used to generate conditional deletion (cOFF) and re-expression (cON) mouse lines because CaMKIIα expression is localized to excitatory neuronal populations, and there is a developmental up-regulation of CaMKIIα expression in pyramidal neurons during second and third postnatal weeks (Burgin et al., 1990). To confirm deletion and re-expression of FMRP in cortical excitatory neurons during the P14-P21 period, we examined the expression of FMRP in AuC at P14, P21, and P60 using immunostaining (Fig. 1). All other analyses were done in adult P60-P70 mice (Supplemental Fig. 1). We analyzed the effects of *Fmr1* deletion and re-expression on PV expression and perineuronal nets (PNN) in adult AuC using immunohistochemistry. EEG recordings were performed in awake, freely moving adult male mice to determine the effects of FMRP deletion and re-expression on neural oscillations in AuC at baseline and in response to sound. Furthermore, we analyzed the activation of PV cells with cFos immunoreactivity. Biochemical measurements of gelatinase activity, PV levels, and TrkB phosphorylation were also done in AuC of both cOFF and cON adult male mice. Finally, we examined anxiety-like behaviors, hyperactivity, and socialization in cOFF and cON adult male mice.

2.3. Mice

Fmr1^{Flox} and *Fmr1*^{FloxNeo} mice were generated in the laboratory of Dr. David Nelson (Baylor College of Medicine, Houston, Texas) (Mientjes et al., 2006). Cre$^{CaMKII\alpha}$ mice (RRID:IMSR_JAX: 005359) were obtained from Jackson Laboratories. To delete FMRP specifically in excitatory neurons during P14-P28 period, we crossed male Cre$^{CaMKII\alpha}$ with female *Fmr1*$^{Flox/Flox}$ mice to produce male Cre$^{CaMKII\alpha}$*Fmr1*$^{Flox/y}$ conditional deletion (cOFF) mice and their control wildtype (Ctrl WT) littermates *Fmr1*$^{Flox/y}$ mice. To re-express FMRP specifically in excitatory neurons during P14-P28 period, we crossed male Cre$^{CaMKII\alpha}$ with female *Fmr1*$^{FloxNeo/FloxNeo}$ mice to produce male Cre$^{CaMKII\alpha}$*Fmr1*$^{FloxNeo/y}$ conditional re-expression (cON) mice and their control knockout (Ctrl KO) littermates *Fmr1*$^{FloxNeo/y}$ mice. All genotypes were confirmed by PCR analysis of genomic DNA isolated from mouse tails. Mice were maintained in an AAALAC accredited facility under a 12 h light/dark cycle (lights on, 0700–1900 h; lights off, 1900–0700 h) and fed standard mouse chow. Food and water were provided to the mice ad libitum. All procedures were approved by IACUC and done according to NIH guidelines.

2.4. Immunofluorescence

Age-matched P14, P21, and P60-70 male Ctrl WT, cOFF, Ctrl KO and cON mice were euthanized with isoflurane and sodium pentobarbital and perfused transcardially first with cold phosphate-buffered saline (PBS, 0.1 M) to clear out the blood and then with 4% paraformaldehyde (PFA) in 0.1 M PBS for fixation. Brains were removed and post-fixed for 2–4 h in 4% PFA. 40-100 μm brain slices were obtained using a vibratome (5100mz Campden Instruments). AuC was identified using hippocampal landmarks and the Franklin and Paxinos mouse brain atlas (Paxinos and Franklin, 2004). For each brain, an average of 5–6 brain slices containing AuC were collected.

2.5. Detection of PV/PNN

Immunostaining in 100 μm brain slices containing AuC was performed as previously described with minor modifications (Lovelace et al., 2020). Briefly, brain slices were post-fixed for an additional 2 h in 4% PFA in 0.1 M PBS and then washed three times in 0.1 M PBS for 10 min. Slices were then quenched with 50 mM ammonium chloride for 15 min and washed three times with PBS for 10 min. Next, brain tissues were permeabilized with 0.1% Triton X-100 in PBS, and nonspecific staining was blocked with a 5% Normal Goat Serum (NGS; Sigma,

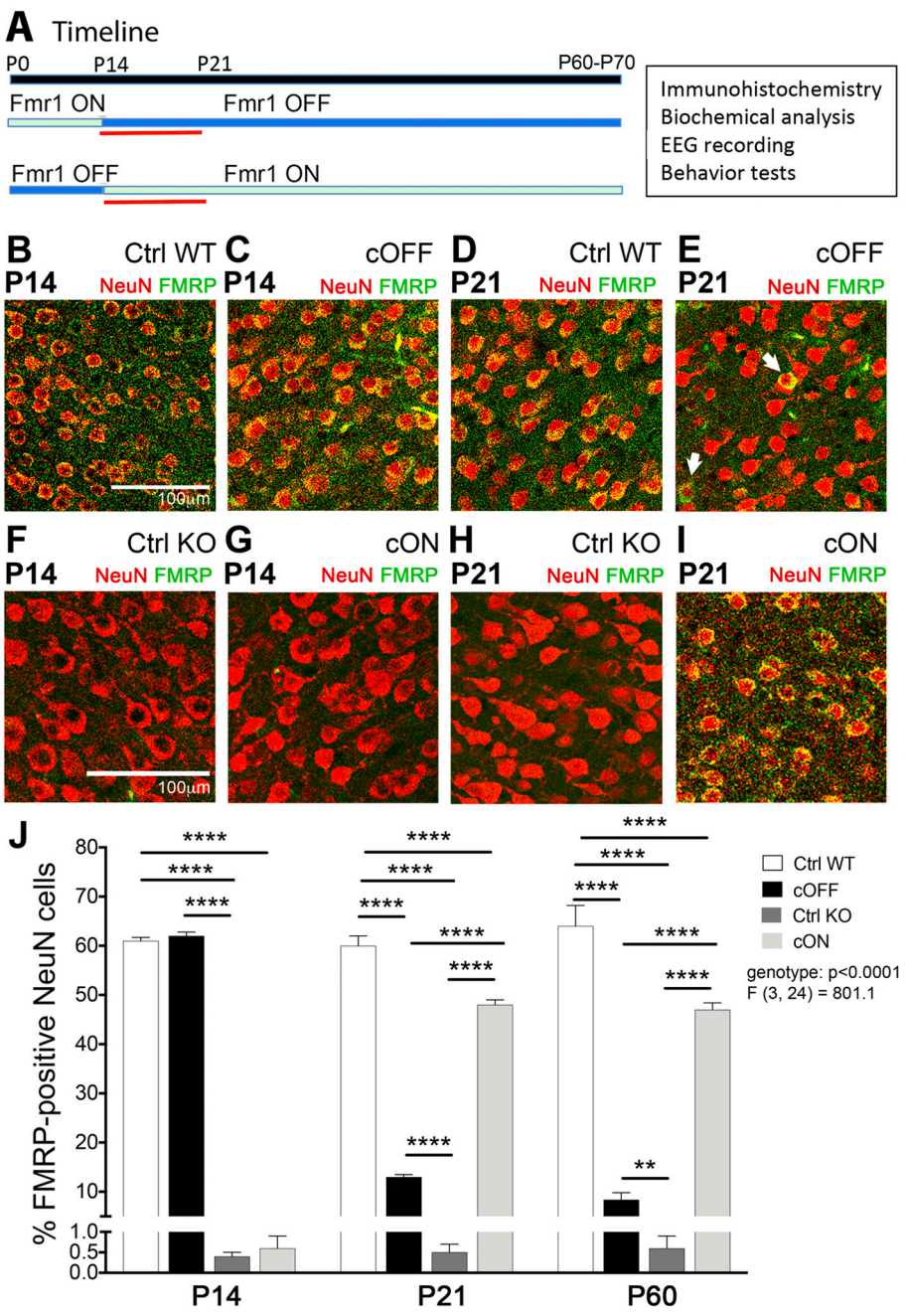

Fig. 1. Deletion and re-expression of *Fmr1* in excitatory neurons occur during the P14-P21 developmental period.

(A) To turn *Fmr1* expression OFF or ON specifically in excitatory neurons during the P14-P21 period, male $Cre^{CaMKII\alpha}$ were crossed with female $Fmr1^{Flox/Flox}$ or $Fmr1^{FloxNeo/FloxNeo}$ mice to produce male $Cre\text{-}^{CaMKII\alpha}Fmr1^{Flox/y}$ conditional deletion (cOFF) or $Cre\text{-}^{CaMKII\alpha}Fmr1^{FloxNeo/y}$ conditional re-expression (cON) mice, respectively. As developmental up-regulation of CaMKIIα expression in pyramidal neurons is observed during the third postnatal week (red line), *Fmr1* deletion or re-expression is expected to occur during the P14-P21 period. FMRP expression was analyzed at P14, P21 and P60. All other experiments, including immunohistochemical, biochemical, EEG, and behavioral experiments were performed at P60-70.

(B–I) Confocal images show NeuN (red) and FMRP (green) immunoreactivity in AuC of Ctrl WT, cOFF, Ctrl KO and cON mice at P14 and P21. (J) Quantitative analysis of the percentage of FMRP-positive NeuN cells. Graphs show mean ± SEM (n = 3 mice/group, two-way ANOVA (Genotype: F (3, 24) = 801.1, $p < 0.0001$; Age: F (2, 24) = 0.4349, p = 0.6524; Interaction: F (6, 24) = 229.9, $p < 0.0001$) followed by Tukey's multiple comparisons post-test, $^{**}p < 0.01$, $^{****}p < 0.0001$; Supplementary Table 1). At P14, no significant differences were observed in the percentage of NeuN+ neurons with FMRP between Ctrl WT and cOFF mice or between cON and Ctrl KO mice. However, at P21 and P60, the percentage of NeuN+ neurons with FMRP decreased in cOFF mice compared to Ctrl WT mice, and increased in cON mice compared to Ctrl KO mice.

catalog# G9023-10 mL) and 1% Bovine Serum Albumin (BSA; Fisher Scientific, catalog# 9048468) in 0.1 M PBS solution. Brain slices were treated overnight with mouse anti-parvalbumin antibody (1:1000; Sigma, catalog# P3088, RRID: AB_477 329) to label parvalbumin-positive (PV) inhibitory interneurons. *Wisteria floribunda* agglutinin (WFA; 4 µg/mL; Vector Laboratories, cat# FL-1351, RRID: AB_2 336,875) in 0.1 M PBS containing 1% NGS, 0.5% BSA, and 0.1% Tween-20 solution was used to stain for PNNs containing aggrecan, known as WFA+ PNNs. WFA is a lectin, which binds glycosaminoglycan side chains of chondroitin sulfate proteoglycan aggrecan that is found in PNNs (Pizzorusso et al., 2002). After overnight incubation, brain slices were washed three times in 0.1 M PBS containing 0.5% Tween-20 for 10 min and incubated with secondary antibody, donkey anti-mouse Alexa 594 (4 µg/mL; Thermo Fisher Scientific, catalog# A-21203, RRID: AB_2 535,789) in 0.1 M PBS for 1 h. Slices were then washed three times with 0.1 M PBS containing 0.5% Tween-20 for 10 min, mounted with Vectashield containing DAPI (Vector Labs, catalog# H-1200, RRID: AB_2336790) and Cytoseal (ThermoScientific, catalog# 8310–16).

2.6. Detection of FMRP expression

Immunostaining for FMRP was performed using antigen retrieval methods, as previously described (Lovelace et al., 2020). Briefly, 40 µm brain slices were mounted onto Superfrost Plus Microscope Charged Slides (Fisher Scientific, catalog #22–034-979); washed 3 times with TBS (0.1 M Tris Cl pH 7.5, 0.15 M NaCl) for 10 min; treated with 0.8% Na Borohydride (Sigma S-9125) to reduce background and autofluorescence; and boiled in 0.01 M Na Citrate (Citric acid, sodium salt in water pH 6.0, Sigma C-8532) to achieve antigen retrieval. Permeabilization was performed with 0.5% Triton-X 100 for 20 min, and slices were stained overnight with mouse anti-FMRP (1:100; Developmental Studies Hybridoma Bank, catalog #2F5-1-s, RRID: AB

_10805421), and rabbit anti-NeuN (1:1000; Abcam, catalog #ab104225, RRID: AB_10711153) in TBS containing 2% Normal Donkey Serum (NDS) and 0.1% Triton-X 100. After incubation with primary antibodies, slices were washed three times in TBS for 10 min and incubated with secondary antibodies for 1 h. Secondary antibodies used were donkey anti-rabbit Alexa 594 (4 μg/mL; Thermo Fisher Scientific, catalog# A-21207, RRID: AB_141637), and donkey anti-mouse Alexa 488 (4 μg/mL; Molecular Probes, catalog# A-21202, RRID: AB_141607). Slices were mounted with Vectashield containing DAPI and Cytoseal.

2.7. Image analysis

Slices were imaged using confocal microscopy (Leica SP5) by collecting a series of 20 high-resolution optical sections (1024 × 1024-pixel format) at 1 μm step intervals (z-stack) that were captured for each slice using a 10×, 20×, or a 63× water-immersion objective (1.2 numerical aperture), with 1× or 2× zoom. All images were acquired under identical conditions. Each z-stack was collapsed into a single image by projection, converted to a TIFF file, encoded for blind analysis, and analyzed using ImageJ. ImageJ was used to identify and manually count PV-positive cells, WFA+ PNN cells, PV/PNN co-localization, NeuN-positive cells, and FMRP/NeuN co-localization. Cortical layers were determined as previously reported (Anderson et al., 2009) and used for layer-specific analysis. Three slices were used per animal, and cell counts were obtained in layers 1–4 of both the right and left AuC (cell density was measured per layer). The freehand selection tool and measure function was used to specify layers of AuC, and the point tool was used to label PNNs, PV cells, and NeuN cells added to the ROI manager. Particle Analysis Cell Counter plugin in Image J was used to count co-localization. Average cell density was calculated for each animal. Statistical analysis was performed with two-way ANOVA followed by Tukey's multiple comparison post-test using GraphPad Prism 6 software (RRID: SCR_002798). Data represent mean ± standard error of the mean (SEM).

2.8. Surgery for in vivo EEG recordings

Age-matched adult P60-70 male cOFF ($n = 10$) and their littermate controls (Ctrl WT; $n = 10$), or adult P60-70 cON ($n = 13$) and their littermate controls (Ctrl KO; $n = 13$) were used for the EEG studies as previously described with modifications (Lovelace et al., 2018; Lovelace et al., 2020). Mice were anesthetized with isoflurane inhalation (0.2–0.5%) and an injection of ketamine and xylazine (K/X) (i.p. 80/10 mg/kg), and then secured in a bite bar and placed in a stereotaxic apparatus (model 930; Kopf, CA). Artificial tear gel was applied to the eyes to prevent drying. Toe pinch reflex was used to measure anesthetic state every 10 min throughout the surgery, and supplemental doses of K/X were administered as needed. Once the mouse was anesthetized, a midline sagittal incision was made along the scalp to expose the skull. A Foredom dental drill was used to drill 1 mm diameter holes in the skull overlying the right auditory cortex (−1.6 mm, +4.8 mm), left frontal lobe (+3.0 mm, −1.6 mm), and left occipital (−4.2 mm, −5.1 mm) (coordinate relative to Bregma: anterior/posterior, medial/lateral). Three-channel electrode posts from Plastics One (MS333-2-A-SPC) were attached to 1 mm stainless steel screws from Plastics One (8L003905201F), and screws were advanced into drilled holes until secure. Special care was taken not to advance the screws beyond the point of contact with the Dura. Dental cement was applied around the screws, on the base of the post, and exposed skull. A triple antibiotic was applied along the edges of the dental cement, followed by an injection of subcutaneous Buprenorphine (0.1 mg/kg). Mice were placed on a heating pad to aid recovery from anesthesia. A second Buprenorphine injection was administered 4 h after surgery, 2 more doses were administered 1-day post-op, and a final dose was administered 2 days post-op. Post-surgery mice were individually housed, returned to the vivarium, and monitored daily until the day of EEG recordings (5 days post-surgery). The separation between the last post-surgical Buprenorphine injection and EEG recordings was 3 days.

2.9. Electrophysiology

Baseline and auditory event-related potential (ERP) recordings were obtained between the hours of 8:00 A.M. and 6:00 P.M. using the BioPac system (BIOPAC Systems, Inc.) from awake and freely moving mice as published previously (Lovelace et al., 2018). Mice were allowed to habituate in the recording chamber for 15 min prior to being connected to the BioPac system. A three-channel tether was attached to the electrode post (implanted during surgery) under brief isoflurane anesthesia. After recovery from isoflurane, the mouse was placed inside a grounded Faraday cage, and the tether was attached to a commutator located directly above the cage. Mice were allowed to habituate for an additional 20 min before EEG recordings were obtained.

The BioPac MP150 acquisition system was connected to two EEG 100C amplifier units (one for each channel) to which the commutator was attached. The lead to the occipital cortex was used as a reference for the frontal cortex (FC) and AuC screw electrodes. The acquisition hardware was set to high-pass (>0.5 Hz) and low-pass (<100 Hz) filters. Normal EEG output data were collected with gain maintained the same (10,000×) between all recordings. Data were sampled at a rate of either 2.5 or 5 kHz using Acqknowledge software and down tested to 1024 Hz post hoc using Analyzer 2.1 (Brain Vision Inc.). Sound delivery was synchronized with EEG recording using a TTL pulse to mark the onset of each sound in a train. Baseline EEGs were recorded for 5 min (no auditory stimuli were presented), followed by recordings in response to auditory stimulation. After these experiments were completed, mice were returned to the colony and euthanized at a later date.

2.10. Acoustic stimulation

All experiments were conducted in a sound-attenuated chamber lined with anechoic foam (Gretch-Ken Industries, OR) as previously described with modifications (Lovelace et al., 2018; Lovelace et al., 2020). Acoustic stimuli were generated using RVPDX software and RZ6 hardware (Tucker-Davis Technologies, FL) and presented through a free-field speaker (MF1 Multi-Field Magnetic Speaker; Tucker-Davis Technologies, FL) located 12 in. directly above the cage. Sound pressure level (SPL) was modified using programmable attenuators in the RZ6 system. The speaker output was ~65-70 dB SPL at the floor of the recording chamber with fluctuation of +/− 3 dB for frequencies between 5 and 35 kHz as measured with a ¼ inch Bruel & Kjaer microphone. Each mouse was exposed to acoustic stimuli for approximately 2 ½ h between the hours of 8:00 A.M. and 6:00 P.M.

We used acoustic stimulation paradigms that have been previously established in *Fmr1* KO mice (Lovelace et al., 2018), which is analogous to work in humans with FXS (Ethridge et al., 2017). A chirp-modulated signal (henceforth, 'chirp') was used to induce and measure stimulus-evoked synchronized oscillations. The chirp is a 2 s broadband noise stimulus with amplitude modulated (100% modulation depth) by a sinusoid whose frequencies increase (up-chirp) or decrease (down-chirp) linearly in the 1–100 Hz range (Artieda et al., 2004; Pérez-Alcázar et al., 2008; Purcell et al., 2004). The chirp facilitates a rapid measurement of transient oscillatory response (delta to gamma frequency range) to auditory stimuli of varying frequencies and can be used to compare oscillatory responses in different groups in clinical and pre-clinical settings (Purcell et al., 2004). Inter-trial coherence analysis (Tallon-Baudry et al., 1996) can then be used to determine the ability of the neural generator to synchronize oscillations to the frequencies present in the stimulus.

The stimulus was ramped in sound level from 0 to 100% over 1 s (rise time) first to avoid contamination of chirp by onset response, which then smoothly transitioned into chirp modulation of the noise. Up- and down-chirp trains were presented 300 times each (for a total of 600 trains).

Both directions of modulation were tested to ensure any frequency-specific effects were not due to the frequency transition history within the stimulus. Up- and down- chirp trains were presented in an alternating sequence. The interval between each train was randomly varied between 1 and 1.5 s.

To study evoked response amplitudes and habituation, trains of 100 ms broadband noise were presented at two repetition rates, 0.25 Hz (a non-habituating rate) and 4 Hz (a habituating rate) (Lovelace et al., 2016). Each train consisted of 10 noise bursts, and the inter-train interval used was 8 s. Each repetition rate was presented 100 times in an alternating pattern (Lovelace et al., 2016). The onset of trains and individual noise bursts were tracked with separate TTL pulses used to quantify response latency.

2.11. EEG data analysis

Data were extracted from Acqknowledge and files saved in a file format (EDF) compatible with BrainVision Analyzer 2.1 software as previously described (Lovelace et al., 2018; Lovelace et al., 2020). All data were notch filtered at 60 Hz to remove residual line frequency power from recordings. EEG artifacts were removed using a semi-automatic procedure in Analyzer 2.1 for all recordings. Less than 20% of data were rejected due to artifacts from any single mouse. Baseline EEG data were divided into 2 s segments, and Fast Fourier Transforms (FFT) were calculated on each segment using 0.5 Hz bins, and then average power (μV^2/Hz) was calculated for each mouse from 1 to 100 Hz. Power was then binned into standard frequency bands: Delta (1–4 Hz), Theta (4-10 Hz), Alpha (10-13 Hz), Beta (13-30 Hz), Low Gamma (30-55 Hz), and High Gamma (65–100 Hz). Responses to chirp trains were analyzed using Morlet wavelet analysis. Chirp trains were segmented into windows of 500 ms before chirp onset to 500 ms after the end of the chirp sound (total of 3 s because each chirp was 2 s in duration). EEG traces were processed with Morlet wavelets from 1 to 100 Hz using complex number output (voltage density, μV/Hz) for Inter Trial Phase Coherence (ITPC) calculations, and power density (μV^2/Hz) for non-phase locked Single Trial Power (STP) calculations for chirp. Analysis of ITPC (voltage density, μV/Hz), and baseline corrected "induced power" density (μV^2/Hz) for on-set and on-going responses to broadband noise trains was also performed. Wavelets were run with a Morlet parameter of 10 as this gave the best frequency/power discrimination. This parameter was chosen since studies in humans found the most robust difference around 40 Hz, where this parameter is centered (Ethridge et al., 2017). To measure phase synchronization at each frequency across trials, Inter Trial Phase Coherence (ITPC) was calculated. The equation used to calculate ITPC is:

$$ITPC(f,t) = \frac{1}{n}\sum_{k=1}^{n}\frac{F_k(f,t)}{|F_k(f,t)|}$$

where f is the frequency, t is the time point, and k is the trial number. Thus, $F_k(f,t)$ refers to the complex wavelet coefficient at a given frequency and time for the kth trial. There were no less than 275 trials (out of 300) for any given mouse after segments containing artifacts were rejected.

2.12. Statistical analysis and definition of movement states

Statistical group comparisons of chirp responses (ITPC and STP) and broadband noise trains (ITPC and induced power) were quantified by wavelet analysis. Analysis was conducted by binning time into 256 parts and frequency into 100 parts, resulting in a 100 × 256 matrix. Non-parametric cluster analysis was used to determine contiguous regions in the matrix that were significantly different from a distribution of 1000 randomized Monte Carlo permutations based on previously published methods (Maris and Oostenveld, 2007). Briefly, if the cluster sizes of the real genotype assignments (both positive and negative direction, resulting in a two-tailed alpha of $p = 0.025$) were larger than 97.25% of the random group assignments, those clusters were considered significantly different between genotypes. This method avoids statistical assumptions about the data and corrects for multiple comparisons.

Because movement can alter cortical gain (Fu et al., 2015; Niell and Stryker, 2010), and *Fmr1* KO mice show hyperactivity, a piezoelectric transducer was placed underneath the recording cage to detect when the mouse was moving. The term 'baseline' is used to indicate EEGs recorded in these mice without any specific auditory stimuli. The term 'still' is used to describe baseline EEG when the mouse was stationary. The term 'moving' is used to describe baseline EEG when the mouse was moving based on a threshold criterion for the piezoelectric signal that was confirmed by analyzing the video recording (under IR light) that was taken throughout the EEG recording procedure. In all cases where genotype means are reported, SEM was used. The genotype differences in baseline power were analyzed on six dependent variables using multivariate one-way analysis of co-variance (MANCOVA) with one covariate (movement), Independent Variables (IV): Genotype (Ctrl WT, cOFF, Ctrl KO, and cON mice), dependent variables (DV): 6 frequency bins (delta to high gamma). The proportion of time spent moving during the 5-min recording session was used as a covariate to isolate the effects of genotype and control for the effect movement has on cortical gain. When multiple comparisons for MANCOVA were made, genotype comparisons were corrected using Bonferroni adjustments. The divisor for Bonferroni correction for multiple comparisons (for six frequency bands) on MANCOVA was set to 6, $\alpha = 0.05/6 = 0.0083$. Data are often expressed and plotted as a ratio of control group values to gauge relative differences in various factors using the same scale.

2.13. cFos analysis

Neuronal activation marker, cFos, was used to examine neural activation under the baseline condition without any specific auditory stimuli (quiet) or after exposure to sound (sound). Age-matched adult (P60-70) male Ctrl WT, cOFF, Ctrl KO and cON mice ($n = 4$ per group) were habituated in a sound-attenuated chamber (Gretch-Ken, OR) for 3 h between 9:00 A.M. and 12:00 P.M. after which they were exposed to either 15 min of silence (quiet) or broadband noise at 65–70 dB SPL (sound). Following exposure, the mice were kept in the sound-attenuated chamber for another 45 min after which they were euthanized with isoflurane and sodium pentobarbital and perfused transcardially between 1:00 P.M. and 1:30 P.M. Brains were removed and post-fixed for 2 h in 4% PFA. 100 μm brain slices were obtained, and immunostaining was performed as described above. Brain slices were treated overnight with mouse anti-parvalbumin antibody (1:500; Sigma, catalog #P3088, RRID: AB_477 329), and rabbit anti-cFos antibody (1:500; Cell Signaling Technology, catalog #2250, RRID: AB_2247211). After primary antibody, brain slices were incubated with secondary antibody, donkey anti-rabbit Alexa 594 (4 μg/mL; Thermo Fisher Scientific, catalog# A-21207, RRID: AB_141637), and donkey anti-mouse Alexa 488 (4 μg/mL; Molecular Probes, catalog# A-21202, RRID: AB_141607) for 1 h. Slices mounted with Vectashield containing DAPI (Vector Labs, catalog# H-1200, RRID: AB_2336790) and Cytoseal (ThermoScientific, catalog# 8310–16). Slices were imaged using confocal microscopy (Leica SP5) as described above. All images were acquired under identical conditions. Image analysis was performed using ImageJ macro plugin PIPSQUEAK (https://labs.wsu.edu/sorg/research-resources/). Slaker, Barnes, et al. (2016), Slaker, Blacktop, et al. (2016), and Slaker, Harkness, et al. (2016) introduced a standardized methodology for analyzing cell density and intensity called PIPSQUEAK. For image analysis, ten images in the *Z*-stack (1.194 pixels/μm) were compiled into a single image using ImageJ macro plugin PIPSQUEAK, scaled, and converted into 32-bit grayscale, TIFF files. PIPSQUEAK was run in "semi-automatic mode" to select ROIs to identify individual PV-positive and cFos-positive cells, as well as PV/cFos co-localization, which were then verified by a trained experimenter who

was blinded to the experimental conditions. The plug-in compiles this analysis to identify single- (Slaker et al., 2016a; Slaker et al., 2016b; Slaker et al., 2016c), double- (Reinhard et al., 2019), and triple-labeled neurons (Harkness et al., 2019) (https://ai.RewireNeuro.com). Distributions of densities and intensities were compared between experimental groups to assess differences in cell densities and intensities between Ctrl WT, cOFF, Crtl KO and cON mice under both conditions (quiet and sound). Statistical analysis was performed with two-way ANOVA (genotype, sound) followed by Tukey's multiple comparison post-test using GraphPad Prism 6 software (RRID: SCR_002798). Data represent mean ± standard error of the mean (SEM).

2.14. Dye-quenched (DQ) Gelatin assay and analysis

The DQ-Gelatin plate assay was used to assess gelatinase activity as described previously (Sidhu et al., 2014; Lovelace et al., 2020; Pirbhoy et al., 2020). A FITC-quenched gelatin peptide that fluoresces following cleavage by gelatinases MMP-2 and MMP-9 was used to measure gelatinase proteolytic activity. Adult (P60) male Ctrl WT and cOFF mice, or Ctrl KO and cON littermates (n = 4–6 mice per group) were euthanized with isoflurane, and AuC was immediately dissected on ice based on coordinates (Paxinos and Franklin, 2004) and previous electrophysiological and dye-placement studies (Martin del Campo et al., 2012). Auditory cortical tissues were re-suspended in ice-cold lysis buffer (50 mM Tris-HCl, pH 7.4, 150 mM NaCl, 5 mM EDTA, 0.05% Triton X-100, and 1 mM PMSF) containing protease inhibitor cocktail (Sigma, cat. # P8340) and phosphatase inhibitor cocktail (Sigma, cat. #P0044). Lysates were measured for total protein concentrations using the BCA colorimetric protein assay (Pierce, cat#23235).

Lysates were diluted in reaction buffer and mixed with a fluorescence-labeled gelatin substrate (Molecular Probes, E12055). Samples were incubated in the dark for 3 h at room temperature. The fluorescence intensity was analyzed using 495 nm excitation wavelength and 515 nm emission wavelength. The signal was measured every 20 min during the 3 h incubation period using a fluorescence microplate reader equipped with standard fluorescein filters (SoftMax Pro). For each time point, background fluorescence intensity was corrected by subtracting the values derived from reaction buffer control. A standard curve to assess gelatinase activity was generated using recombinant mouse MMP-9 (rmMMP-9, approximately 1500 pmol/min/μg, R&D Systems, cat. #909-MM-010). A linear regression of rmMMP-9 activity (standard curve) and relative gelatinase activity based on the average fluorescence intensity of five replicates was used to assess gelatinase proteolytic activity in the brain samples. Statistical analysis was performed with one-way ANOVA followed by Tukey's multiple comparison post-test using GraphPad Prism 6 software (RRID: SCR_002798). Data represent mean ± standard error of the mean (SEM).

2.15. Western blot analysis

Adult (P60) male Ctrl WT, cOFF, Ctrl KO and cON mice were euthanized with isoflurane between 9:00 A.M and 12:00 P.M., and following euthanization AuC was immediately dissected from each mouse (n = 4 mice per group), cooled in PBS, and homogenized in ice-cold lysis buffer (50 mM Tris-HCl, pH 7.4, 150 mM NaCl, 5 mM EDTA, 0.05% Triton X-100, and 1 mM PMSF) containing protease inhibitor cocktail (Sigma, cat. #P8340) and phosphatase inhibitor cocktail (Sigma, cat. #P0044). The samples were processed as previously described with modifications (Nikolakopoulou et al., 2016; Koeppen et al., 2018; Lovelace et al., 2020). The samples were rotated at 4 °C for at least 1 h to allow for complete cell lysis and then cleared by centrifugation at 13,200 rpm for 15 min at 4 °C. Supernatants were isolated and boiled in reducing sample buffer (Laemmli 2× concentrate, S3401, Sigma), and separated on 8–16% Tris-Glycine SDS-PAGE precast gels (EC6045BOX, Life Technologies). Proteins were transferred onto Protran BA 85 Nitrocellulose membrane (GE Healthcare) and blocked for 1 h at room temperature in 5% skim milk (catalog #170–6404, Bio-Rad). Primary antibody incubations were performed overnight at 4 °C with antibodies diluted in TBS/0.1% Tween-20/5% BSA. The following primary antibodies were used: mouse anti-PV (Millipore, catalog #MAB1572, RRID: AB_2174013); rabbit anti-βactin at 1:2000 (1:2000; Abcam, catalog #ab8227, RRID: AB_2305186); mouse anti-total TrkB (1:2000; BD Transduction Laboratories, catalog #610101, RRID: AB_397507); and rabbit anti-phospho-TrkB (Tyr515) (Bioworld, catalog #AP0236). For primary antibodies from Cell Signaling Technology a dilution of 1:1000 was used, unless stated otherwise.

Blots were washed 3 × 10 min with TBS/0.1% Tween-20 and incubated with the appropriate HRP-conjugated secondary antibodies for 1 h at room temperature in a TBS/0.1% Tween-20/5% BSA solution. The secondary antibodies used were HRP-conjugated donkey anti-mouse IgG (Jackson ImmunoResearch, catalog #715–035–150, RRID: AB_2340770) or HRP-conjugated goat anti-rabbit IgG (Jackson ImmunoResearch, catalog #111–035-003, RRID: AB_2313567). After secondary antibody incubations, blots were washed three times for 10 min in TBS/0.1% Tween-20, incubated in ECL 2 Western Blotting Substrate (Thermo Scientific, catalog #80196), and a signal was collected with CL-XPosure film (Thermo Scientific, catalog #34090). For re-probing, membrane blots were washed in stripping buffer (2% SDS, 100 mM β-mercaptoethanol, 50 mM Tris-HCl, pH 6.8) for 30 min at 55 °C, then rinsed repeatedly with TBS/0.1% Tween-20, finally blocked with 5% skim milk, and then re-probed. Developed films were then scanned, and band density was analyzed by measuring band and background intensity using Adobe Photoshop CS5.1 software (RRID:SCR_014199). Four samples per group (Ctrl WT and cOFF or Ctrl KO and cON) were run per blot, and precision/tolerance (P/T) ratios for cOFF and cON samples were normalized to P/T ratios of Ctrl WT and Ctrl KO samples, respectively. Statistical analysis was performed with an unpaired t-test using GraphPad Prism 6 software. Data represent mean ± standard error of the mean (SEM).

2.16. Behavioral assessments

Adult (P60-P70) mice were tested first in open-field and elevated plus-maze (in that order), followed by a three-chamber test. All tests were done in a brightly lit room (650 lx), between 9:00 A.M. and 2:00 P.M.

3. Open-field test

Anxiety-like behaviors and locomotor activity were tested in the open-field test as described previously (Lovelace et al., 2020). P60-P70 Ctrl WT (n = 8) and cOFF (n = 7), or Ctrl KO (n = 8) and cON (n = 8) littermate mice were tested between the hours of 9:00 A.M. and 1:00 P.M., and open-field test was always performed prior to the elevated plus-maze. A 72 × 72-cm open-field arena with 50-cm-high walls was constructed from opaque acrylic sheets with a clear acrylic sheet for the bottom. The open-field arena was placed in a brightly lit room, and one mouse at a time was placed in the corner of the open field and allowed to explore for 10 min while being recorded with digital video from above. There was no adaptation time as the test was performed to measure anxiety and locomotor activity during mouse response to a novel environment. The floor was cleaned with 2–3% acetic acid, 70% ethanol, and water between tests to eliminate odor trails. The arena was subdivided into a 4 × 4 grid of squares, with the middle of the grid defined as the center. A line, 4 cm from each wall, was added to measure thigmotaxis. Locomotor activity was scored by analyzing speed of mouse using TopScan Lite software (Clever Sys., Inc., VA), and the time in thigmotaxis was used to indicate anxiety. The analysis was performed in 5 min intervals for the total 10 min exploration duration. Assessments of the digital recordings were performed blind to the condition. Statistical analysis was performed with one-way ANOVA followed by Tukey's multiple comparison post-test using GraphPad Prism 6 software (RRID:

SCR_002798). Data represent mean ± standard error of the mean (SEM).

4. Elevated plus-maze

Anxiety-like behaviors and locomotor activity were also tested in the elevated plus-maze test as described previously (Lovelace et al., 2020). P60-P70 Ctrl WT ($n = 8$) and cOFF ($n = 7$), or Ctrl KO ($n = 8$) and cON ($n = 8$) littermate mice were tested between the hours of 9:00 A.M. and 1:00 P.M. The elevated plus-maze consisted of four arms in a plus configuration. Two opposing arms had 15-cm tall walls (closed arms), and two arms were without walls (open arms). The entire maze sat on a stand 1 m above the floor. Each arm measured 30 cm long and 10 cm wide. Mice were allowed to explore the maze for 10 min while being recorded by digital video from above. Similar to the open-field test there was no adaptation time in the elevated plus-maze as well. The maze was wiped with 2–3% acetic acid, 70% ethanol, and water between each test to eliminate odor trails. This test was always done following the open-field test. TopScan Lite software was used to measure the percent of time spent in open arms and speed. The time spent in the open arm was used to evaluate anxiety-like behavior, while speed was measured to assess overall locomotor activity (Lovelace et al., 2020). The analysis was performed in 5 min intervals for the 10 min exploration duration. Assessments of the digital recordings were done blind to the condition using TopScan Lite software. Statistical analysis was performed with one-way ANOVA followed by Tukey's multiple comparison post-test using GraphPad Prism 6 software (RRID: SCR_002798). Data represent mean ± standard error of the mean (SEM).

5. Social novelty test

Sociability and social novelty preference were tested in P60-P70 Ctrl WT ($n = 8$) and cOFF ($n = 7$), or Ctrl KO (n = 8) and cON (n = 8) littermate mice using a three-chamber test as described previously with minor modifications (Nguyen et al., 2020). Briefly, a rectangular box contained three adjacent chambers 19 × 45 cm each, with 30-cm-high walls and a bottom constructed from transparent Plexiglas. The three chambers were separated by dividing walls, which were made from transparent Plexiglas with openings between the middle chamber and each side chamber. Removable doors over these openings permitted chamber isolation or free access to all chambers. All testing was done in a brightly lit room (650 lx), between 9:00 A.M. and 2:00 P.M. Before testing, mice were housed in a room with a 12 h light/dark cycle with ad libitum access to food and water. The cages were transferred to the behavioral room 30 min before the first trial began for habituation. The test mouse was placed in the central chamber with no access to the left and right chambers and allowed to habituate to the test chamber for 5 min before testing began. Session 1 measured sociability; in Session 1, another mouse (Stranger 1) was placed in a wire cup-like container in one of the side chambers. The opposite side had an empty cup of the same design. The doors between the chambers were removed, and the test mouse was allowed to explore all three chambers freely for 10 min, while being digitally recorded from above. The following parameters were monitored: the duration of direct contact between the test mouse and either the stranger mouse or empty cup and the time spent in each chamber. Session 2 measured social memory; in Session 2, a new mouse (Stranger 2) was placed in the empty wire cup in the second side chamber. Stranger 1, a now-familiar mouse, remained in the first side chamber. The test mouse was allowed to freely explore all three chambers for another 10 min, while being recorded, and the same parameters were monitored. The placement of Stranger 1 in the left or right chamber was randomly altered between trials. The floor of the chamber was cleaned with 2%–3% acetic acid, 70% ethanol, and water between tests to eliminate odor trails. Assessments of the digital recordings were done using TopScan Lite software (Clever Sys., Inc., VA). To measure changes in sociability and social novelty preference, the percent time spent in each chamber was calculated in each test. Further, a sociability index = time in S1 chamber/(time in S1 chamber + time in the empty chamber) and social novelty preference index = time in S2 chamber/(time in S2 chamber + time in S1 chamber) were calculated as described previously (Nguyen et al., 2020; Nygaard et al., 2019). For the sociability index, values <0.5 indicate more time spent in the empty chamber, >0.5 indicate more time spent in the chamber containing Stranger 1, and 0.5 indicates an equal amount of time in both chambers. For the social novelty preference index, values <0.5 indicate more time spent in the chamber containing Stranger 1 or familiar mouse, >0.5 indicate more time spent in the chamber containing Stranger 2 or new stranger mouse, and 0.5 indicates an equal amount of time in both chambers. Statistical analysis for time spent in each chamber was performed using two-way ANOVA followed by Tukey's multiple comparison post-test. Statistical analysis for sociability index and social novelty preference index was performed with one-way ANOVA followed by Tukey's multiple comparison post-test using GraphPad Prism 6 software (RRID: SCR_002798). Data represent mean ± standard error of the mean (SEM).

6. Results

6.1. Deletion and re-expression of Fmr1 in excitatory neurons during the P14-P21 developmental period

To achieve the deletion of FMRP from excitatory neurons during the P14-P21 period, we crossed male $Cre^{CaMKII\alpha}$ with female $Fmr1^{Flox/Flox}$ mice and analyzed the expression of FMRP at P14, P21 and P60 in $Cre^{CaMKII\alpha}$ /$Fmr1^{Flox/y}$ (cOFF) and their littermate controls, $Fmr1^{Flox/y}$ (Ctrl WT) mice (Fig. 1A). Ctrl WT mice showed FMRP expression in NeuN+ cells in AuC at P14 (Fig. 1B) and P21 (Fig. 1D). FMRP expression was also detected in NeuN+ cells in AuC of cOFF mice at P14 (Fig. 1C). However, FMRP immunoreactivity was visibly reduced in AuC of cOFF mice by P21 (Fig. 1E). There was a significant decrease in NeuN+ neurons with FMRP in the cOFF mice compared to Ctrl WT mice at P21 and P60 (Fig. 1J; Supplementary Table 1). It was not surprising to see a small number of NeuN+ cells maintaining FMRP immunoreactivity (arrow, Fig. 1E), as not all neurons express CaMKIIa, in particular GABAergic neurons (Tamamaki et al., 2003). FMRP immunoreactivity was also visible in NeuN-negative cells, most likely astrocytes. These data confirm that FMRP was deleted from cortical excitatory neurons in AuC during the P14-P21 developmental window and the deletion was maintained in adult P60 cOFF mice.

To achieve the re-expression of FMRP in cortical excitatory neurons during the same P14-P21 period, we crossed male $Cre^{CaMKII\alpha}$ with female $Fmr1^{FloxNeo/FloxNeo}$ mice and analyzed the expression of FMRP at P14, P21and P60 in $Cre^{CaMKII\alpha}$ /$Fmr1^{FloxNeo/y}$ (cON) and their littermate controls, $Fmr1^{FloxNeo/y}$ (Ctrl KO) mice (Fig. 1A). Ctrl KO mice showed no FMRP expression in NeuN+ cells at P14 (Fig. 1F) and P21 (Fig. 1H). FMRP expression was also not detected in NeuN+ cells of cON mice at P14 (Fig. 1G). However, FMRP immunoreactivity was observed in AuC of cON mice by P21 (Fig. 1I). There was a significant increase in NeuN+ neurons with FMRP in the cON mice compared to Ctrl KO mice at P21 and P60 (Fig. 1J; Supplementary Table 1). However, the number of NeuN+ neurons with FMRP in the cON mice was lower than in Ctrl WT mice, as FMRP re-expression under CaMKIIa promoter targeted only excitatory neurons. These data confirm that FMRP was re-expressed in cortical excitatory neurons during the P14-P21 developmental window in AuC and FMRP expression was also maintained in adult P60 cON mice (Fig. 1J; Supplementary Table 1).

6.2. Deletion and re-expression of Fmr1 in excitatory neurons during P14-P21 postnatal period affect PV and PNN cell density in adult AuC

We examined PV and WFA+ PNN-containing cell density in AuC of adult (P60-P70) Ctrl WT ($n = 6$), cOFF (n = 6), Ctrl KO ($n = 4$), and cON ($n = 5$) mice (Fig. 2A-G). Similar to what we had previously seen in the adult global *Fmr1* KO mice (Lovelace et al., 2020), there was a

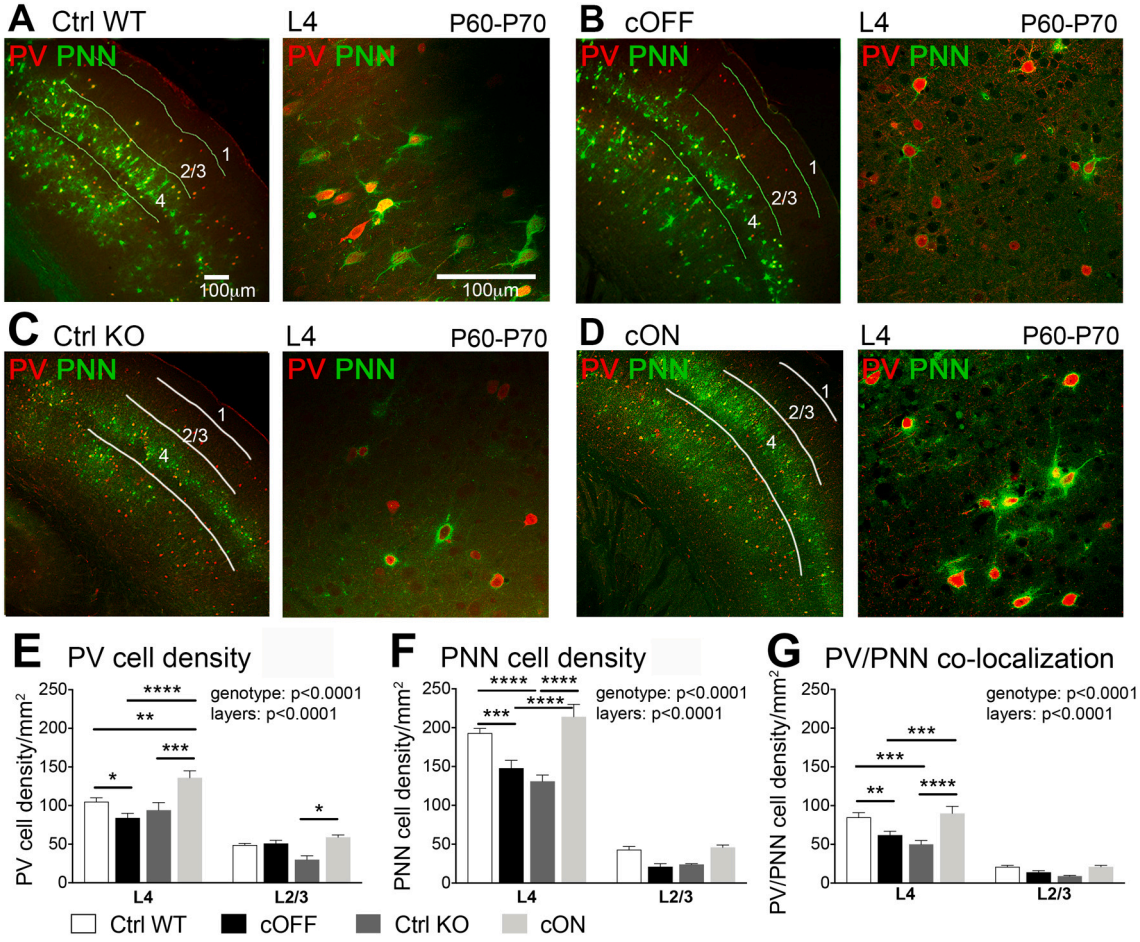

Fig. 2. Postnatal deletion and re-expression of *Fmr1* in excitatory neurons affect the density of PV cells, WFA+ PNNs, and PV/PNN co-localization in the adult mouse AuC.

(A-D) Confocal images show PV immunoreactivity (red) and WFA+ PNN labeling (green) in AuC of adult (P60-P70) Ctrl WT (A), cOFF (B), Ctrl KO (C), and cON (D) mice with representative low magnification (left panels in A-D) and high magnification images (right panels in A-D). Scale Bars pertain to all panels.

(E-G) Quantitative analysis of the density of PV, PNN, or PV/PNN positive cells. Graphs show mean ± SEM (n = 4–6 mice/group, two-way ANOVA (genotype, layer) followed by Tukey's multiple comparison post-test *$p < 0.05$, **$p < 0.01$, ***$p < 0.001$, ****$p < 0.0001$; Supplementary Table 2). (E) PV cell density was significantly lower in L4 but not L2/3 AuC of cOFF compared to Ctrl WT. Conversely, PV cell density was significantly higher in both L4 and L2-3 AuC of cON than Ctrl KO (Genotype: $F(3, 34) = 14.78$, $p < 0.0001$; Layers: $F(1, 34) = 200.4$, $p < 0.0001$; Interaction: $F(3, 34) = 5.176$, $p = 0.0047$). (F) PNN cell density was significantly lower in L4 but not L2/3 AuC of cOFF and Ctrl KO compared to Ctrl WT, but significantly higher in cON compared to Ctrl KO and cOFF (note that only WFA+ cells were counted to measure PNN density) (Genotype: $F(3, 34) = 20.25$, $p < 0.0001$; Layers: $F(1, 34) = 594.7$, $p < 0.0001$; Interaction: $F(3, 34) = 5.532$, $p = 0.0033$). (G) PV/PNN co-localization was also significantly lower in L4 but not L2/3 AuC of cOFF and Ctrl KO compared to Ctrl WT, and significantly higher in cON than Ctrl KO and cOFF (G) (Genotype: $F(3, 34) = 13.03$, $p < 0.0001$; Layers: $F(1, 34) = 262$, $p < 0.0001$; Interaction: $F(3, 34) = 3.693$, $p = 0.0210$).

significant decrease in PV cell density, WFA+ PNN cell density, and PV/PNN co-localization in AuC of cOFF mice compared to their littermate Ctrl WT mice in L4 but not in L2/3 (Fig. 2E-G; Supplementary Table 2). Conversely, there was a significant increase in PV cell density, WFA+ PNN cell density, and PV/PNN co-localization in AuC of cON mice compared to their littermate Ctrl KO mice in L4, and L2/3 only showed a significant increase in PV cell density (Fig. 2E-G; Supplementary Table 2). WFA+ PNN cell density and PV/PNN co-localization was also significantly lower in L4 AuC of Ctrl KO compared to Ctrl WT mice and was normalized in cON to Ctrl WT levels (Fig. 2F, G; Supplementary Table 2). These data indicate that postnatal deletion of FMRP from excitatory neurons is sufficient to reduce PV expression and associated PNNs in L4. In contrast, the re-expression of FMRP in excitatory neurons during the same period is sufficient to prevent abnormal phenotypes. Thus, expression of FMRP in excitatory neurons before P14-P21 might not be required for the normal development of PV expression in cortical inhibitory interneurons. We next tested if functional recovery was also possible by re-expressing FMRP in forebrain excitatory neurons during the P14-21 window.

6.3. Baseline EEG gamma power is significantly altered in adult AuC following postnatal deletion and re-expression of Fmr1

If impaired PNN and PV expression in AuC underlie abnormal neural oscillations observed in the global *Fmr1* KO mice, then we should see similar deficits in cOFF mice, and a reversal of those abnormal phenotypes in cON mice. To test this hypothesis, we measured electrocortical activity in cOFF and cON mice using EEG recordings. Baseline (no sound simulation) EEG power spectral density was calculated in P65-P70 AuC of Ctrl WT ($n = 10$) and cOFF (n = 10) mice, or Ctrl KO ($n = 13$) and cON (n = 13) littermate male mice from EEGs recorded during a five-min period. Examples of 1 s segments of baseline EEG for each genotype, as well as genotype averages (+/− SEM) of power spectra, are depicted in Fig. 3. Even in the raw traces (Fig. 3A), enhanced high-frequency oscillations are apparent in AuC of cOFF mice compared to Ctrl WT, while high-frequency oscillations appear to be reduced in AuC of cON mice compared to Ctrl KO. The group average power spectral densities are shown in Fig. 3B, wherein genotype differences (Ctrl WT vs. cOFF and Ctrl KO vs. cON) in AuC can be seen at ~40 Hz frequencies (Fig. 3B).

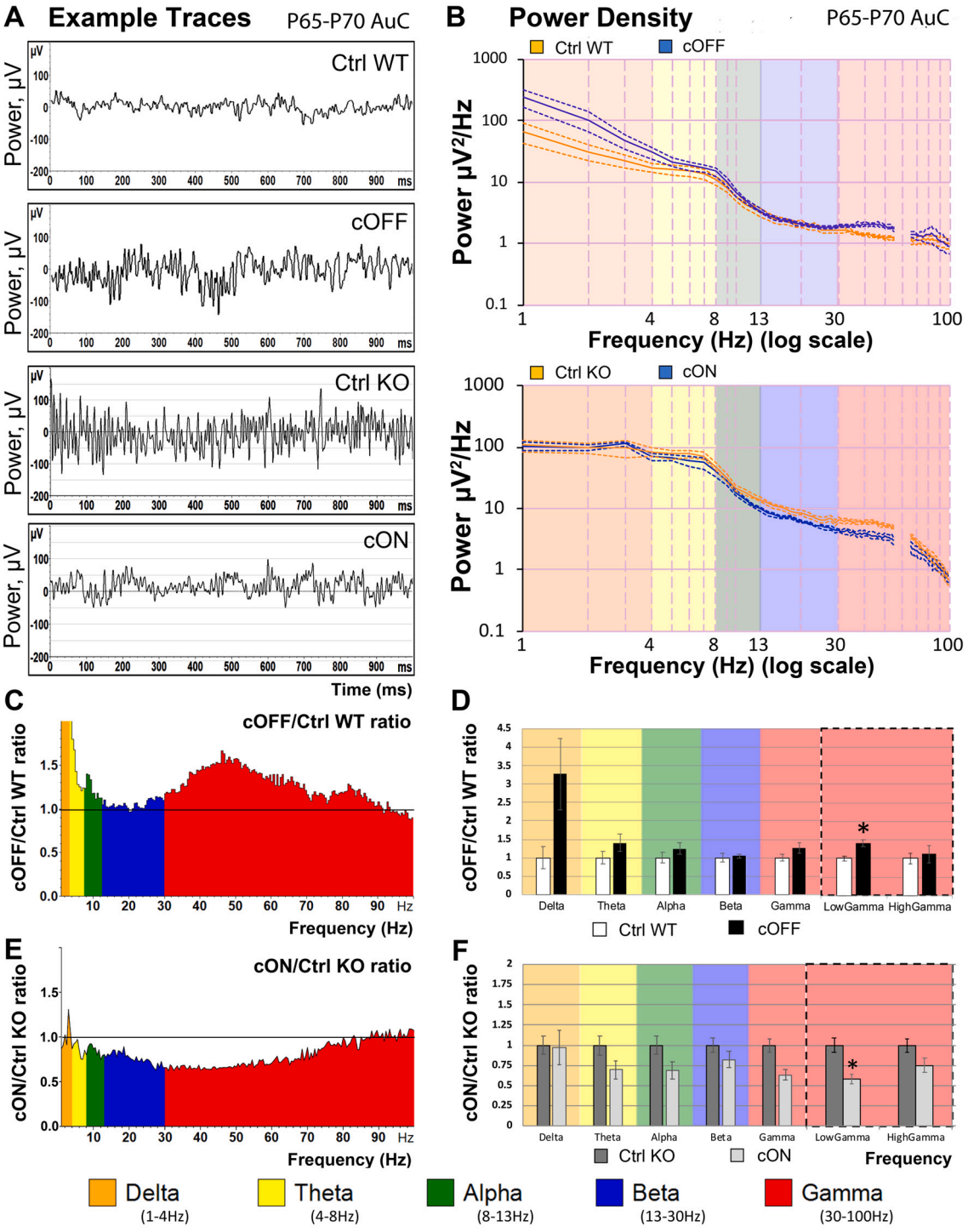

Fig. 3. Characterization of baseline EEG power in AuC of cOFF and cON mice.
Five min of baseline EEG data (in the absence of auditory stimulation) from electrodes implanted in P60-P65 AuC of Ctrl WT ($n = 10$) and cOFF (n = 10), or Ctrl KO (n = 13) and cON (n = 13) littermate mice was recorded at P65-P70, and FFT analysis was done to determine spectral power. (A) Examples of 1 s segments of raw baseline EEG from AuC of Ctrl WT and cOFF or Ctrl KO and cON littermates. The enhanced high-frequency oscillations can be qualitatively observed in the cOFF and Ctrl KO mice, compared to the Ctrl WT and cON mice, respectively. (B) Power density (μV^2/Hz) was calculated for each artifact-free segment using Fast Fourier Transform, followed by averaging all segments for a given mouse. These individual averages then contributed to the genotype grand average for each genotype (n = 10–13 per genotype). Significant differences between genotypes are observed in AuC at low-gamma (30-55 Hz) frequencies. Frequencies 55-65 Hz were excluded in *all* analyses, as a 60 Hz notch filter was utilized to eliminate line noise. (C, D) Average power in the cOFF and cON mouse AuC is expressed as the ratio of control levels (Ctrl WT and Ctrl KO, respectively). A value of 1 (horizontal black line) indicates no mean difference in power at that frequency between genotypes, while values above the black line indicate cOFF>Ctrl WT or cON>Ctrl KO, and below the black line indicates cOFF<Ctrl WT or cON<Ctrl KO. The high low-gamma power in the cOFF mice relative to Ctrl WT and the reduced low-gamma power in the cON relative to Ctrl KO can be visualized in these plots. (E, F) Quantification of spectral power differences across genotype pairs. AuC values were divided into canonical frequency bands. MANCOVA analysis controlling for the effect of movement revealed differences in the low-gamma range of AuC after Bonferroni correction for multiple comparisons (Ctrl WT and cOFF: low-gamma, $F(1,17) = 9.042$, $p = 0.0079$, $\eta^2 = 0.35$; Ctrl KO vs. cON: low-gamma, $F(1,23) = 14.992$, $p = 0.001$, $\eta 2 = 0.395$; $^*p < 0.008$).

Statistical analysis was performed using a one-way MANCOVA approach with percentage time spent moving as a covariate. We compared genotype mean differences on six bands: Delta (1–4 Hz), Theta (4-10 Hz), Alpha (10-13 Hz), Beta (13-30 Hz), Low gamma (30-55 Hz), and High Gamma (65–100 Hz). The gamma band (30–100 Hz) was divided because low (30–60 Hz) versus high frequency (>60 Hz) bands in gamma range may arise from different mechanisms (Balakrishnan and Pearce, 2014; Dvorak and Fenton, 2014; Ray and Maunsell, 2011). We confirmed assumptions of equality of covariance using Box's M, $p = 0.080$ (for Ctrl WT vs. cOFF) and $p = 0.153$ (for Ctrl KO vs. cON). For Ctrl WT vs. cOFF mice, Levene's test of equality of error variance showed the only difference between genotypes in the delta band of the cOFF group ($p = 0.003$). Therefore further analysis of delta was not carried out. We report an effect of genotype (Ctrl WT vs. cOFF: Pillai's Trace = 0.709, $p = 0.010$; Ctrl KO vs. cON: Pillai's Trace = 0.513, $p = 0.027$) across all 6 of the combined frequency variables, which include movement as a covariate. We then determined that the only individual frequency band difference between genotypes in AuC of cOFF and cON mice was in the low-gamma band (Fig. 3C-F).

Low-gamma power in the AuC was significantly different between genotypes after correction for multiple comparisons (Ctrl WT and cOFF: low-gamma, $F(1,17) = 9.042$, $p = 0.0079$, $\eta^2 = 0.35$; Ctrl KO vs. cON: low-gamma, $F(1,23) = 14.992$, $p = 0.001$, $\eta 2 = 0.395$, Supplementary Table 3). These data suggest that deletion of FMRP after P14 is sufficient to cause enhanced power of resting low-gamma oscillations in the adult AuC of cOFF mice. Significantly, this phenotype can be reversed with the re-expression of *Fmr1* in the mouse brain after the second postnatal week. In addition, beneficial effects of re-expression of FMRP only in excitatory neurons suggest that these cells play a critical role in controlling low-gamma oscillations, most likely by influencing the development of PV interneurons.

6.4. Postnatal deletion and re-expression of Fmr1 affect gamma synchronization to dynamic acoustic stimuli in adult AuC

Abnormal PV neuron function is predicted to cause abnormal sound-evoked gamma synchronization. We tested this by recording EEGs in response to a dynamic stimulus called chirp, which evokes synchronized oscillations to a dynamic frequency sweep signal. After repeated chirp presentations (300 trials for up, 300 for down), the inter-trial phase coherence (ITPC) was calculated across trials in the time X frequency domain using Morlet Wavelet analysis. After grand average ITPC was calculated for each group, means for Ctrl WT mice ($n = 10$) were subtracted from the means for cOFF mice (n = 10), and means for Ctrl KO mice ($n = 13$) were subtracted from the means for cON mice (n = 13) (Fig. 4A-B; only 'up' chirp data are shown). For statistical comparisons, non-parametric cluster analysis was used to determine contiguous regions in the time X frequency domain statistically different between genotypes (Fig. 4A-B). For statistical analysis, clusters of p-values were calculated, and significant differences ($p < 0.025$) were overlaid on the chirp response to demonstrate quantitative differences between each group after correction for multiple comparisons (Lovelace et al., 2020). Monte Carlo statistical method on cluster analysis revealed a significant decrease in low-gamma band ITPC in AuC of cOFF mice centered ~55 Hz (Fig. 4B, top panel). Conversely, we observed a significant increase of the low-gamma band ITPC in AuC of cON mice in ~40-55 Hz range (Fig. 4B, bottom panel). Because the direction of frequency change in the sound (up chirp or down chirp) did not affect the findings, results are presented only for up chirp. These data indicate that postnatal deletion of FMRP is sufficient to trigger the gamma synchronization deficits similar to what is observed in AuC of germline *Fmr1* KO mice (Lovelace et al., 2018). Notably, the phenotype was reversed by re-expression of FMRP after P14 and only in excitatory neurons, suggesting that abnormal communications between excitatory and inhibitory neurons may contribute to the impaired sound-evoked gamma synchronization in AuC of *Fmr1* KO mice.

6.5. Postnatal deletion and re-expression of Fmr1 in excitatory neurons affect background gamma power in mouse AuC during chirp stimulation

Next, we investigated non-phase locked STP during the chirp stimulation period (Fig. 4C-D) because any increase in gamma power during the duration of acoustic stimulation is predicted to decrease the ability of the neural generators to produce temporally consistent responses to the dynamic chirp stimulus. In addition, increased STP is seen in the global *Fmr1* KO mouse (Lovelace et al., 2018) and humans with FXS (Ethridge et al., 2017). Using the same statistical cluster analysis as for the chirp ITPC, the cOFF mice showed a significant increase in background gamma power in AuC and only in the low-gamma band (Fig. 4D, top panel). In contrast, the cON mice showed a significant decrease in background gamma power in AuC in the low-gamma band (Fig. 4D, bottom panel).

Taken together, these data suggest that normal expression of FMRP in excitatory neurons is necessary to establish resting, evoked, and background gamma oscillations in AuC, most likely through their interactions with fast-spiking inhibitory interneurons. In addition, FMRP deletion or expression during the P14-P21 period is sufficient to manipulate gamma power, suggesting that the development of normal gamma oscillations in auditory cortical circuits begins to occur during this time window.

6.6. Induced power and ITPC to sound onset are differentially regulated in AuC of cOFF and cON mice

We compared evoked responses to trains of brief (100 ms) broadband noise stimuli (10 noise stimuli per train, 65–70 dB SPL, 100 repetitions of each train). We tested both a habituating rate of sound presentation (4 Hz repetition rate) and a non-habituating repetition rate (0.25 Hz) (Lovelace et al., 2016; Lovelace et al., 2020). Example traces are shown for the first stimulus in the 0.25 Hz train for Ctrl WT and cOFF (Fig. 5A) or Ctrl KO and cON (Fig. 5G) and the first 4 stimuli in the 4 Hz train for Ctrl WT and cOFF (Fig. 5D) or Ctrl KO and cON (Fig. 5J). We measured both ITPC and induced power (baseline corrected) for each repetition rate. In cOFF mice, the ITPC for 0.25 Hz rate showed a statistically significant increase in phase-locking in the beta to low-gamma range (~20-40 Hz) during sound onset (Monte Carlo statistical method on cluster analysis; $p < 0.025$) (Fig. 5B; Supplementary Fig. 2A). This suggests that cOFF mice show elevated synchrony compared to Ctrl WT mice at those specific frequencies. When analyzing phase locking to sound for cON mice compared to Ctrl KO mice, we observed no changes in the beta (20-30 Hz) range. Still, a significant increase in gamma (30-80 Hz) range was observed (Fig. 5H; Supplementary Fig. 2E), consistent with improved phase locking in the gamma band with the chirp stimuli (Fig. 4B). In addition, while cOFF mice displayed a significant increase in induced power during the sound onset (0-100 ms) from the beta to low-gamma range (~20-40 Hz) (Fig. 5C; Supplementary Fig. 2B), cON mice showed a decrease in induced power during sound onset with significant changes in gamma 30-100 Hz range (Fig. 5I; Supplementary Fig. 2F). These results show increased power during sound onset in cOFF mice and decreased power in cON mice, with no significant difference in long latency or "on-going" activity after the initial sound onset (Rotschafer and Razak, 2013).

Analysis of the first four responses to a 4 Hz train of sounds reveals the same ITPC increase to the first sound in the train in the beta/low-gamma (~25-35 Hz) range (Fig. 5E; Supplementary Fig. 2C) in cOFF mice compared to Ctrl WT, with an additional increase in ITPC to the second sound in the train centered ~80 Hz (Fig. 5E; Supplementary Fig. 2C). We observed an increase in phase-locking to the first sound in cON mice compared to Ctrl KO within the gamma 30-80 Hz range with no significant changes in the beta range (Fig. 5K; Supplementary Fig. 2G). The increase in power also centered ~30 Hz during first sound onset (0-100 ms) in cOFF mice (Fig. 5F; Supplementary Fig. 2D), but the power around 30 Hz was significantly downregulated during first and

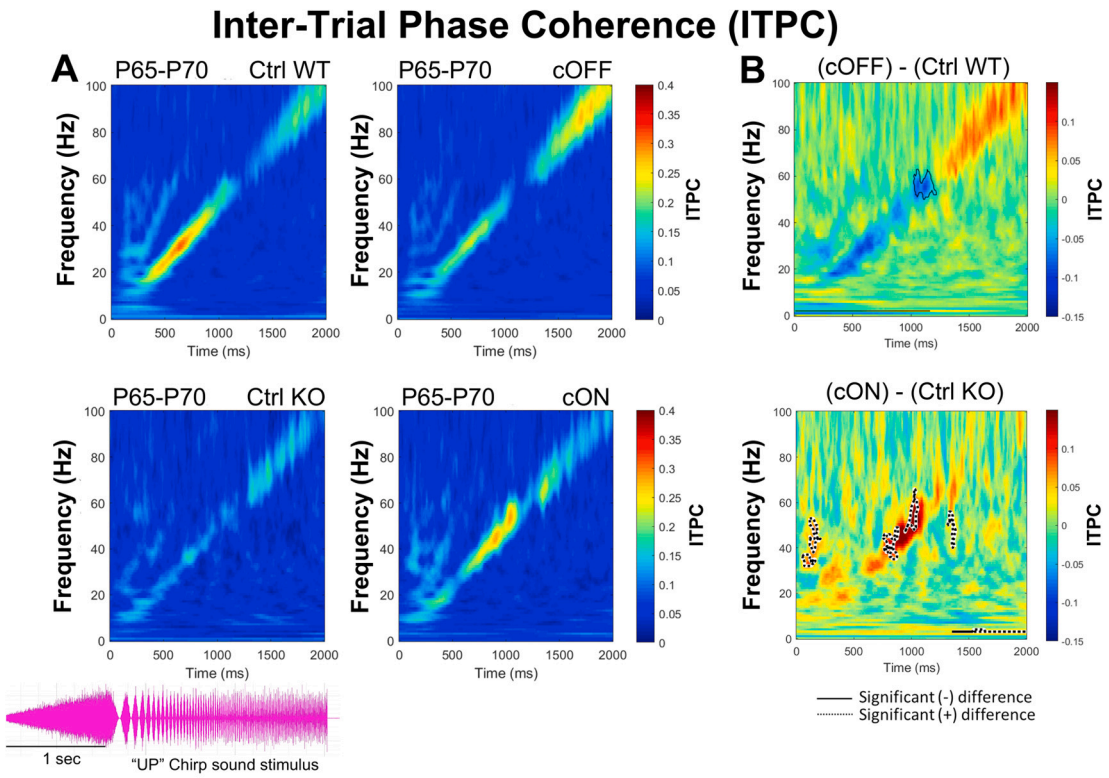

(caption on next page)

second sound onset in cON mice (Fig. 5L; Supplementary Fig. 2H). Interestingly, global KO mice (Ctrl KO) showed high on-going non-phase power after sound onset, which was not observed in cOFF mice (Supplementary Fig. 2B—D and 2F—H). There was a trend for suppression of the on-going power following FMRP re-expression in cON mice (Fig. 5L; Supplementary Fig. 2F—H). The suppression of on-going oscillation power is visually apparent in the example traces shown in Fig. 5J, where the cON mouse shows lower amplitude oscillations throughout the sound train, compared to Ctrl KO mice.

These results indicate elevated synchrony of sound-evoked responses in the beta frequency range when FMRP is deleted from excitatory neurons during postnatal development but no changes in gamma band synchrony. In contrast, gamma synchronization to sound was improved when FMRP expression was restored during the same period. In

Fig. 4. Postnatal deletion or re-expression of *Fmr1* affects phase locking to time-varying auditory stimuli (chirps), as well as non-phase locked background STP. The chirp stimulus (oscillogram shown at the bottom of this figure) is a 1 s broadband noise whose amplitude is modulated linearly by a frequency sweep with frequencies increasing from 1 to 100 Hz. To reduce the effect of early response, the chirp was preceded by a 1 s slow ramp of broadband noise. The ability of AuC neural generators of EEG to follow this temporally dynamic stimulus was quantified by measuring the inter-trial phase coherence (ITPC, also known as phase locking factor). Trains of chirp stimuli were presented to each mouse 300 times. For each mouse, ITPC was measured to determine the degree of phase-locking across trials. (A, B) Grand average matrices were calculated for each genotype (A), and then Ctrl WT ($n = 10$) and Ctrl KO ($n = 13$) ITPC values were subtracted from cOFF (n = 10) and cON (n = 13) values, respectively (B). B, Blue areas indicate cOFF<Ctrl WT, green areas no difference, and red cON>Ctrl KO. Statistical cluster analysis reveals contiguous time x frequency regions that are significantly different between genotypes. Black solid contours (mean negative difference) and black dashed contours (mean positive difference) indicate clusters with significant differences ($p < 0.025$). After subtraction and cluster analysis Monte Carlo statistical method on cluster analysis revealed a significant decrease ($p < 0.025$) in ITPC at low-gamma frequencies (50–60 Hz, blue) in AuC of cOFF mice (B, top panel). Conversely, cluster analysis revealed a statistically significant increase ($p < 0.025$) in ITPC at low-gamma frequencies (~40–60 Hz, red) in AuC of cON mice (B, bottom panel). (C, D) For each mouse, STP was measured to determine the average total non-phase locked power during chirp train presentation. STP represents on-going 'background' power during auditory stimulation. Grand average matrices were calculated for each genotype (C), and then Ctrl WT (n = 10) and Ctrl KO (n = 13) STP values were subtracted from cOFF (n = 10) and cON (n = 13) values, respectively (D). D, Statistical cluster analysis reveals contiguous time x frequency regions that are significantly different between genotypes ($p < 0.025$). Consistent with the low-gamma power changes in baseline EEGs, Monte Carlo statistical method on cluster analysis revealed a statistically significant increase ($p < 0.025$) in STP throughout the sound presentation in the low-gamma range (~40-60 Hz, red) in AuC of cOFF mice (D, top panel), while cON mice express a statistically significant decrease ($p < 0.025$) in STP throughout the sound presentation in the low-gamma range (~40-60 Hz, blue) (D, bottom panel).

addition, induced power was higher during sound onset in cOFF mice with no changes in on-going response, while re-expression of FMRP suppressed the power of both onset and on-going responses following sound presentation.

6.7. Deletion and re-expression of Fmr1 in excitatory neurons during postnatal development affect activation of PV cells in adult AuC

Impaired PNN development can lead to reduced excitability of cortical PV cells resulting in increased network excitation. It is possible that altered gamma oscillations in FXS may arise from dysfunction of PV interneurons, and awakening of PV cells is responsible for enhanced sound-evoked gamma synchronization in cON mice. To test this hypothesis, we examined the density of cFos-expressing cells, overall cFos levels and cFos/PV co-localization in AuC at baseline (quiet; Fig. 6A-D) and 45 min following the 15-min exposure to broadband noise at 65-70 dB (sound; Fig. 6A-D).

In cOFF mice, the density of cFos-positive cells and cFos levels (intensity of cFos immunoreactivity) were significantly higher in L1-4 AuC of cOFF and Ctrl KO mice compared to Ctrl WT mice, and lower in cON mice compared to Ctrl KO and cOFF mice at baseline (quiet, Fig. 6E,F; Supplementary Table 4). However, after exposure to sound, the overall density of cFos-positive cells and cFos levels were similar between genotypes (sound, Fig. 6E,F; Supplementary Table 4). This observation is most likely due to a significant increase in cFos cell density and intensity in Ctrl WT and cON mice but not cOFF and Ctrl KO mice following sound exposure. We next analyzed cFos levels in PV cells and found fewer PV cells expressed cFos, and lower cFos levels in PV cells in L1-4 AuC of cOFF and Ctrl KO mice compared to Ctrl WT mice, and higher in cON mice compared to Ctrl KO and cOFF mice at baseline (quiet, Fig. 6G-H; Supplementary Table 4). After exposure to sound, still fewer PV cells showed cFos immunoreactivity, and cFos levels in PV cells remained lower in cOFF and Ctrl KO mice compared to Ctrl WT mice, and higher in cON compared to Ctrl KO mice (sound, Fig. 6G-H; Supplementary Table 4). There was a significant increase in the percentage of cFos-positive PV cells and cFos levels in PV cells in sound-exposed Ctrl WT, cOFF, Ctrl KO and cON mice when compared to respective quiet condition groups.

These data indicate that reduced PV cell activation may underlie the alterations in auditory processing in cOFF mice. Notably, postnatal re-expression of FMRP only in excitatory neurons during the period of PV cell maturation might be sufficient to promote PV cell activation and restore EEG responses in cON mice.

6.8. Postnatal deletion and re-expression of Fmr1 in excitatory neurons affect gelatinase activity, PV levels, and TrkB phosphorylation in adult AuC

As enhanced MMP-9 activity may contribute to the loss of PNNs by cleaving the extracellular matrix (ECM), we performed a gelatinase activity assay. A significant increase in gelatinase activity was observed in AuC of cOFF and Ctrl KO mice compared to their Ctrl WT counterparts (Fig. 7A; Supplementary Table 5). Conversely, a significant decrease in gelatinase activity was observed in cON mice compared to Ctrl KO and cOFF mice (Fig. 7A; Supplementary Table 5). Consistent with the changes in PV cell density, PV levels were significantly decreased in cOFF and increased in cON mice compared to their respective controls (Fig. 7C, D; Supplementary Table 5). As previous studies have implicated TrkB signaling in PV cell development and survival, we evaluated total TrkB (tTrkB) levels. We found no changes in tTrkB levels in AuC of cOFF or cON mice compared to Ctrl WT or Ctrl KO, respectively (Fig. 7C, F; Supplementary Table 5). However, further analysis revealed lower levels of phosphorylated (i.e., active) form of TrkB (Y515) in AuC of cOFF mice compared to Ctrl WT (Fig. 7C, E; Supplementary Table 5). In contrast, higher levels of phosphorylated TrkB (Y515) were detected in AuC of cON mice compared to Ctrl KO (Fig. 7C, E; Supplementary Table 5).

Together, our results indicate that postnatal deletion of FMRP from excitatory neurons is sufficient to enhance gelatinase activity but reduces PV levels and TrkB phosphorylation in P60 AuC. In contrast, postnatal re-expression of FMRP in only excitatory neurons is sufficient to reverse the deficits in P60 AuC of *Fmr1* KO mice.

6.9. Postnatal deletion and re-expression of Fmr1 in excitatory neurons affect anxiety-like behaviors, locomotor activity, and socialization in adult mice

Cortical hyperexcitability resulting from aberrant PV cell development is also observed in several ASD mouse models (Lee et al., 2017). It may underlie ASD-like behaviors, such as impaired social behaviors, and enhanced anxiety and hyperactivity. Moreover, the changes we see in AuC may not be exclusive to this area of the brain. Therefore, adult (P60-P70) male Ctrl WT ($n = 8$), cOFF mice ($n = 7$), Ctrl KO (n = 8) and cON mice (n = 8) were tested for hyperactivity and anxiety-like behaviors in an elevated plus-maze and open field test (Fig. 8; Supplementary Table 6). cOFF mice exhibited increased anxiety-like behaviors by spending significantly less time in open arms (elevated plus-maze) and a significantly more time in thigmotaxis (open field test) than Ctrl WT mice, suggesting higher anxiety (Fig. 8A,C; Supplementary Table 6). In addition, cOFF and Ctrl KO mice demonstrated increased locomotor activity by showing higher speed than Ctrl WT mice in both elevated

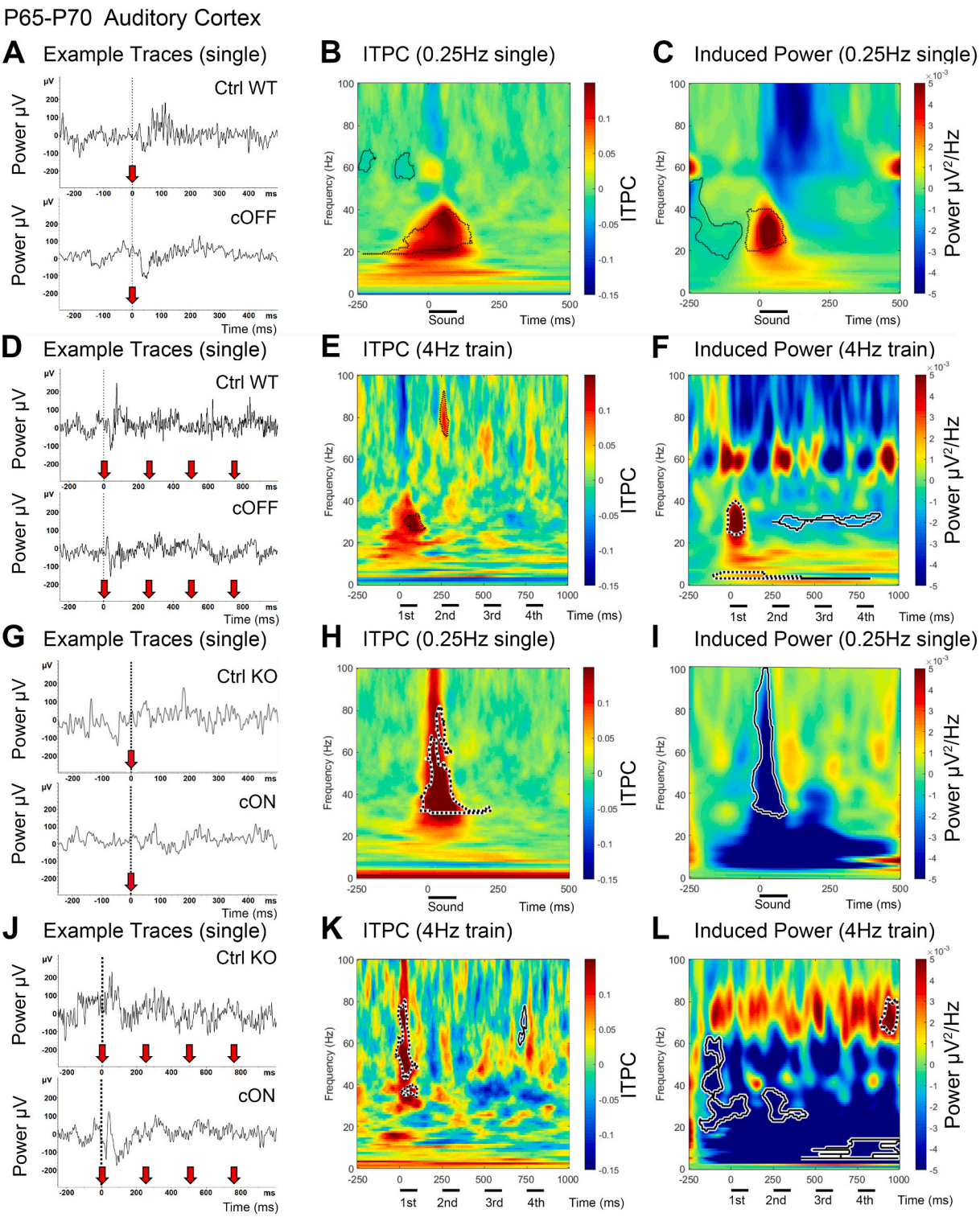

(caption on next page)

plus-maze and open field test (Fig. 8B, D; Supplementary Table 6). In contrast, cON mice exhibited decreased anxiety-like behaviors by spending significantly more time in open arms and a lower time in thigmotaxis than Ctrl KO and cOFF mice (Fig. 8A, C; Supplementary Table 6). cON mice also demonstrated lower locomotor activity with significantly lower speed than Ctrl KO and cOFF mice (Fig. 8B, D; Supplementary Table 6).

Sociability and social novelty preference were assessed using a three-chamber test in adult (P60-70) male Ctrl WT (n = 8), cOFF (n = 7), Ctrl KO (n = 8) and cON (n = 8) mice. cOFF mice had a significantly lower sociability index and spent less time in the chamber with a stranger mouse than Ctrl WT (Fig. 8E; Supplementary Table 6). The social novelty preference index was also significantly lower in cOFF mice that spent less time with a novel mouse than Ctrl WT (Fig. 8F; Supplementary

Fig. 5. Postnatal deletion and re-expression of *Fmr1* affect sound-induced power (baseline corrected) and ITPC in adult AuC.
(A) Example traces in response to sound presentations at 0.25 Hz for Ctrl WT and cOFF mice. Red arrow indicates the onset of 100 ms broadband noise. (B) Grand average difference plot of ITPC during sound presentations between genotypes (cOFF – Ctrl WT). Average plots of each genotype are shown in Supplementary Fig. 2. Black solid contours (mean negative difference) and black dashed contours (mean positive difference) indicate clusters with significant differences ($p < 0.025$). Monte Carlo statistical method on cluster analysis revealed a significant increase ($p < 0.025$) in ITPC in the cOFF mice ~20-40 Hz during the sound presentation. (C) Baseline corrected sound-induced power was calculated for each genotype (Supplementary Fig. 2), and then Ctrl WT values were subtracted from cOFF values. Increased induced power is observed in response to the sound ($p < 0.025$), indicating increased onset activity but no differences at longer latencies after the sound presentation. (D) Example traces of responses to broadband noise train presented at 4 Hz for Ctrl WT and cOFF mice. (E) Significant ITPC differences were observed for the first sound in the train in the same range as seen in B ($p < 0.025$). (F) Increased induced power is observed during the onset of the ERP response in the 20-40 Hz range ($p < 0.025$). (G) Example traces in response to single sound presentations at 0.25 Hz for Ctrl KO and cON mice. (H) Grand average difference plot of ITPC during sound presentations between genotypes (cON – Ctrl KO). There is an increase in ITPC in the cON mice ~30-80 Hz immediately after the sound presentation ($p < 0.025$). (I) Baseline corrected sound-induced power was calculated for each genotype, and then Ctrl KO values were subtracted from cON values. Induced power was decreased during the onset of the ERP response, indicating decreased onset activity ($p < 0.025$). (J) Example traces of 4 Hz sound presentation for Ctrl KO and cON mice. (K) ITPC differences were observed for the first sound in the train in the same range as seen in the single response in H ($p < 0.025$). (L) Decreased induced power ~ 20-40 Hz was observed after the first and second sound presentations, decreased induced power ~ 4-20 Hz was observed after the third and fourth sound presentations ($p < 0.025$).

Table 6). Conversely, both sociability index and social novelty preference were higher in cON mice compared to Ctrl KO and cOFF mice (Fig. 8E, F; Supplementary Table 6). Our findings establish that the P14-P21 deletion of FMRP from excitatory neurons is sufficient to increase anxiety-like behaviors and locomotor activity and decrease socialization. In contrast, FMRP re-expression during the same period is sufficient to reduce anxiety-like behaviors and locomotor activity, and increase socialization in adult mice.

7. Discussion

Cortical hyperexcitability may underlie sensory hypersensitivity that is frequently observed in individuals with FXS and other ASDs and is recapitulated in mouse models of the disorders. Our studies in the mouse model of FXS provide novel insights into (1) how the changes during the postnatal P14-P21 period of PV cell maturation contribute to cortical deficits observed in *Fmr1* KO mice; (2) the role of excitatory neurons in regulating inhibitory PV interneurons during this postnatal development in *Fmr1* KO mice; and (3) whether re-expression of FMRP in only excitatory neurons during the same period is sufficient to ameliorate deficits. We show that *Fmr1* deletion in excitatory neurons during the P14-P21 critical developmental window of PV cell maturation recapitulates some deficits observed in germline *Fmr1* KO mice, including reduced PV expression and activity of PV cells, impaired responses to sound, and behavior deficits. The increased gelatinase activity may contribute to these deficits by cleaving PNNs and affecting communication between excitatory and PV cells during the critical developmental period of PV cell maturation. Importantly, our data show that restoration of *Fmr1* expression in cortical excitatory during the same developmental period prevents the development of these abnormal cellular, electrophysiological and behavioral phenotypes in mice (Fig. 9).

The significant results of the present study point to the sufficiency of postnatal re-expression of *Fmr1*, and only in excitatory neurons, to reverse structural, functional, and behavioral deficits in the *Fmr1* KO mice. As gene reactivation to treat FXS is receiving increasing attention (Hampson et al., 2019; Shitik et al., 2020; Tabolacci et al., 2016; Vershkov et al., 2019), our results suggest the benefits of FMRP re-expression during P14-P21 period of cortical experience-dependent plasticity in mice, which roughly corresponds to the first three years of human life, when symptoms of ASD first emerge in infancy (Contractor, 2021). The cortical hyperexcitability commonly seen in global *Fmr1* KO mice and individuals with FXS may arise from dysfunction across multiple brain regions expressing FMRP and spanning the brainstem to the forebrain. The present results with excitatory neuron-specific removal or re-expression of FMRP using CaMKIIα promoter primarily target cortical pyramidal neurons, indicating that cell-targeted reactivation may produce benefits in physiological responses and behaviors (Gatto and Broadie, 2008; Siegel et al., 2017). As activation of CaMKIIα promoter using reporter mice is primarily observed in L2/3 of AuC with a lower expression in L4 (Supplementary Fig. 3) (Wang et al., 2013), L2/3 excitatory neurons may influence the development and maturation of PV and PNN-expressing cells in L4. However, our study doesn't rule out the involvement of the midbrain. Excitatory neurons in the rostral or caudal portion of the external nucleus of the inferior colliculus are also shown to express GFP under CaMKIIα promoter (Wang et al., 2013), suggesting a possible role of subcortical structures in deficits observed in AuC of cOFF mice.

Altered auditory processing in individuals with FXS and *Fmr1* KO animals suggests that development and plasticity in the auditory system may be affected in FXS (Chen and Toth, 2001; Miller et al., 1999; Nielsen et al., 2002). Multiple studies support the notion that impaired development during the critical postnatal period of circuit refinement may be responsible for abnormal sensory responses in FXS, which could then lead to impaired development of higher cognitive functions, such as language learning (Kim et al., 2013; LeBlanc and Fagiolini, 2011). The shaping of acoustic representations in primary AuC is profoundly influenced by early experience (de Villers-Sidani et al., 2007; Insanally et al., 2009; Popescu and Polley, 2010; Zhang et al., 2001). Exposure of young animals to sensory input refines the balance of excitation and inhibition (Dorrn et al., 2010; Kulinich et al., 2020; Sun et al., 2010), resulting in the receptive field and sensory map reorganization and a long-lasting impact on sound perception (Han et al., 2007). Cortical inhibition and excitation become correlated in mouse AuC by the third postnatal week, with the frequency tuning of the inhibitory component of the receptive fields becoming narrower during the P14-P21 period in a sensory experience-dependent manner (Dorrn et al., 2010). Experience-dependent developmental plasticity is impaired in AuC of global *Fmr1* KO mice (Kim et al., 2013) and may correlate with the development of hyperexcitability seen during the P14-P21 period in these mice (Wen et al., 2018). Our results show that manipulation of FMRP, only in excitatory neurons, during this developmental window (P14-P21), can either disrupt or restore AuC function and indicate that embryonic or early postnatal (P0-P14) re-expression may not be required to normalize sensory hypersensitivity in FXS. Future studies will examine whether the re-expression of FMRP in adulthood will provide the same benefits.

Converging evidence suggests that the loss or dysfunction of PV inhibitory interneurons may contribute to cortical deficits (Gibson et al., 2008; Contractor et al., 2015; Goel et al., 2018; Nomura et al., 2017; Selby et al., 2007; Wen et al., 2018). However, the mechanism is still unclear. It is imperative to identify the sources of PV cell dysfunction and which developmental stage to target, such as neurogenesis, migration, or maturation. Our findings provide novel insight into the cellular mechanism underlying the normalization of cortical function following re-expression of FMRP and emphasize the role of the handshake between excitatory and inhibitory PV neurons during the developmental refinements of cortical networks. Many symptoms of FXS can be linked to a reduced GABAergic inhibition, which has been suggested to lead to an

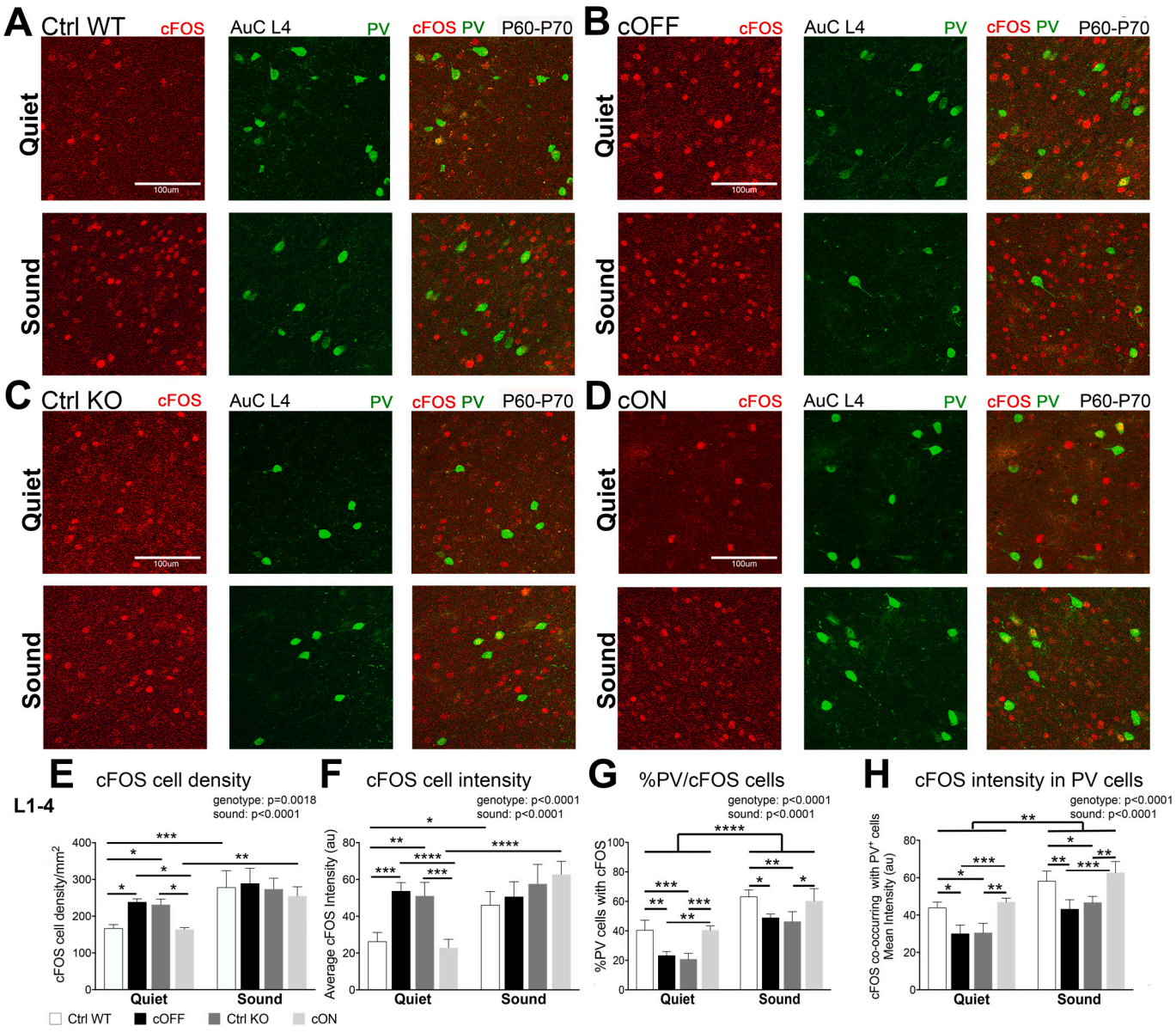

Fig. 6. Postnatal deletion and re-expression of *Fmr1* differentially alter neuronal activity and PV cell activation in adult AuC.

(A-D) Confocal images showing PV (green) and cFOS (red) expression in L4 AuC of adult Ctrl WT (A), cOFF (B), Ctrl KO (C), and cON (D) mice after being exposed to either silence (quiet) or broadband noise at 65-70 dB (sound) for 15 min. Scale Bars pertain to all images in panels A-D.

(E, F) Quantitative analysis of cFOS+ cell density (E) and cFOS intensity (F) in L1-4 AuC. Graphs show mean ± SEM (n = 4/group, two-way ANOVA (cFOS+ cell density - Genotype: F (3, 24) = 6.787, p = 0.0018; Sound: F (1, 24) = 63.67, p < 0.0001; Interaction: F (3, 24) = 2.602, p = 0.0754; cFOS cell intensity - Genotype: F (3, 24) = 11.32, p < 0.0001; Sound: F (1, 24) = 40.03, p < 0.0001; Interaction: F (3, 24) = 13.85, p < 0.0001) followed by Tukey's multiple comparison post-test *p < 0.05; **p < 0.01; ***p < 0.001; ****p < 0.0001; Supplementary Table 4). Under the quiet condition, cFOS+ cell density (E) and cFOS intensity (F) were significantly increased in cOFF mice compared to Ctrl WT but reduced in cON compared to Ctrl KO. Following sound exposure, cFOS+ cell density and cFOS intensity were significantly increased in sound-exposed Ctrl WT mice and cON mice, but not in sound-exposed cOFF and Ctrl KO mice compared to their corresponding quiet groups. However, no significant changes were observed in cFOS cell density and c-FOS intensity between sound-exposed Ctrl WT and cOFF or sound-exposed Ctrl KO and cON mice.

(G, H) Quantitative analysis of %PV cells with cFOS, and cFOS intensity in PV cells in L1-4 AuC. Graphs show mean ± SEM (n = 4/group, two-way ANOVA (% PV cells with cFOS cells - Genotype: F (3, 24) = 25.44, p < 0.0001; Sound: F (1, 24) = 155.6, p < 0.0001; Interaction: F (3, 24) = 0.5509, p = 0.6524; cFOS intensity in PV cells - Genotype: F (3,23) = 30.1, p < 0.0001; Sound: F (1,23) = 79.59, p < 0.0001; Interaction: F (3, 23) = 0.1838, p = 0.9063) followed by Tukey's multiple comparison post-test *p < 0.05; **p < 0.01; ***p < 0.001; ****p < 0.0001; Supplementary Table 4). %PV cells with cFOS (G) and cFOS intensity in PV cells (H) were significantly reduced in cOFF mice than Ctrl WT and increased in cON mice compared to Ctrl KO mice in both quiet condition and after sound exposure. %PV cells with cFOS and cFOS intensity in PV cells were significantly increased in sound-exposed mice compared to quiet groups for all genotypes.

increased ratio of excitation to inhibition (E/I) (Hussman, 2001), another probable cause for impaired cortical maturation (Rubenstein and Merzenich, 2003). Parvalbumin interneurons receive both intracortical and thalamic excitatory inputs, which develop during the cortical critical period (Chittajallu and Isaac, 2010; Daw et al., 2007). There is a significant delay in the formation of excitatory contacts onto fast-spiking interneurons, which likely has a substantial impact on the integration of feedforward inhibitory circuits in the developing somatosensory cortex of *Fmr1* KO mice (Nomura et al., 2017). Previous studies also suggest that FMRP expression in excitatory neurons is

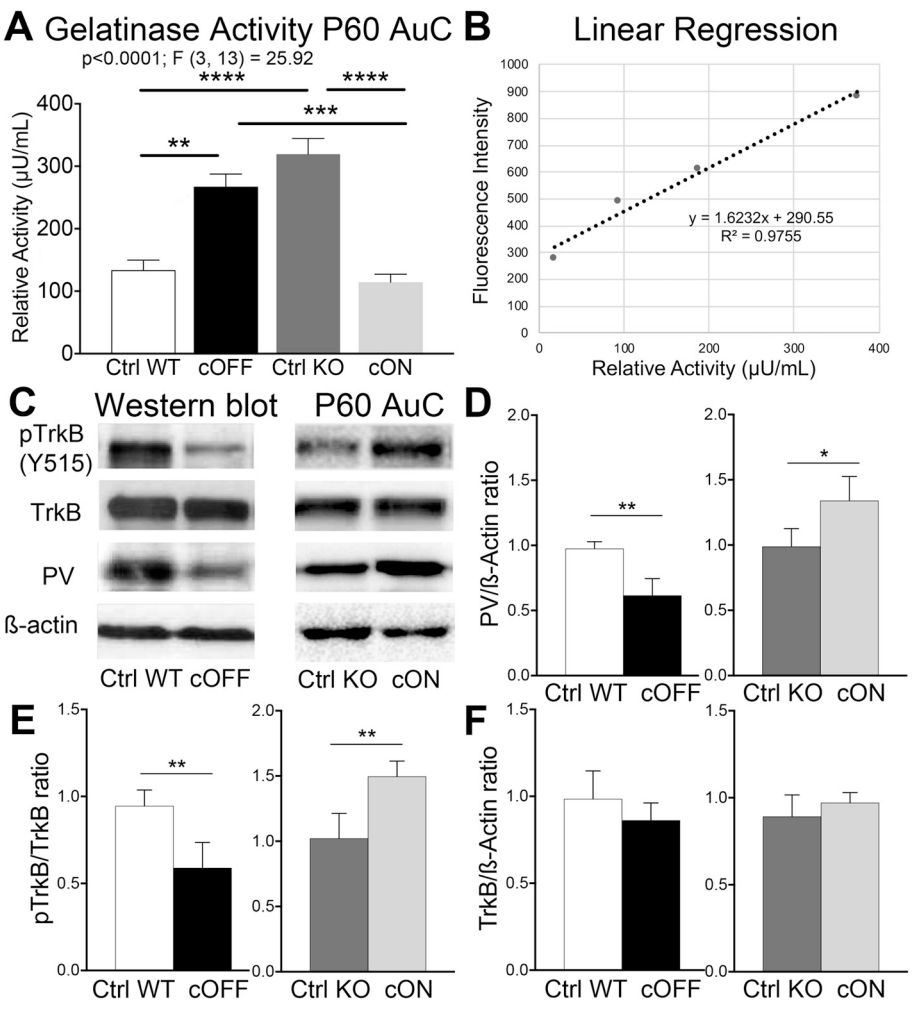

Fig. 7. Gelatinase activity, PV levels, and TrkB phosphorylation are altered in AuC of adult cOFF and cON mice.

(A) Relative gelatinase activity in AuC of adult (P60) Ctrl WT (n = 4), cOFF (n = 5), Ctrl KO (n = 4), and cON (n = 4) mice. Graphs show mean ± SEM (**p < 0.01; ***p < 0.001; ****p < 0.0001, one-way ANOVA (F (3,13) = 25.92, p < 0.0001) followed by Tukey's multiple comparisons post-test; Supplementary Table 5). Gelatinase activity is elevated in AuC of cOFF and Ctrl KO mice compared to Ctrl WT but lower in cON mice than in Ctrl KO and cOFF. (B) Standard curve showing gelatinase activity of recombinant MMP-9 (mean ± SEM).

(C) Western blots showing total PV, TrkB, p-TrkB (Y515), and actin levels in lysates from adult (P60) AuC of Ctrl WT, cOFF, Ctrl KO, and cON mice. Protein levels for cOFF and cON samples were normalized to their respective controls Ctrl WT and Ctrl KO samples. Blots were first probed for PV and then striped and re-probed for p-TrkB(Y515), TrkB, and actin (in that order). (D) Quantitative analysis of PV levels normalized to actin. Graphs show mean ± SEM (n = 4/group, t-test *p < 0.05; **p < 0.01; Supplementary Table 5). PV levels are significantly reduced in adult AuC of cOFF mice and increased in cON mice compared to their control counterparts. (E) Quantitative analysis of p-TrkB(Y515)/TrkB ratios. Graphs show mean ± SEM (n = 4/group, t-test **p < 0.01; Supplementary Table 4). p-TrkB(Y515)/TrkB ratio is significantly decreased in AuC of cOFF mice and up-regulated in cON mice compared to their control counterparts. (F) Quantitative analysis of total TrkB levels normalized to actin. No significant changes were observed in total TrkB levels in AuC of both cOFF and cON mice compared to their respective controls.

required for normal cortical activity (Hays et al., 2011) and show that embryonic FMRP loss in cortical excitatory neurons is sufficient to affect the development of PV inhibitory interneurons (Lovelace et al., 2020). The reduction in PV expression in cOFF mice may occur due to reduced excitatory drive onto these neurons (Gibson et al., 2008). Our current study indicates that these deficits are seen following the removal of FMRP during the P14-P21 period when connections are established between excitatory and inhibitory neurons. Moreover, we observed a reduced cFos immunoreactivity in PV cells of cOFF mice, suggesting that a common mechanism across sensory cortices in *Fmr1* KO mice is reduced excitation/activation of PV cells. Strikingly, the increase in PV expression and cFos immunoreactivity in PV cells in cON mouse AuC further reinforces the idea that expression of FMRP in excitatory neurons might be required during the postnatal period of normal network development, in particular PV cells.

Enhanced MMP-9 activity observed in cOFF mice may also disrupt the communications between excitatory and PV cells by degrading aggrecan-containing WFA+ PNNs. In the cerebral cortex, PNN loss around PV cells reduces the excitability of these cells (Balmer, 2016; Lensjø et al., 2017; Wen et al., 2018). PNNs protect PV cells from oxidative stress, and the loss of PNNs may lead to PV cell death (Cabungcal et al., 2013). Therefore, degradation of PNN is predicted to decrease the excitability of PV cells leading to hyperexcitability of cortical networks and abnormal neural oscillations. Conversely, the increase of PNNs and reduction in gelatinase activity observed in cON mice following FMRP re-expression coincided with increased density of PV cells, enhanced PV cell activity, and improved responses to sound assessed with EEG.

Our findings show EEG phenotypes in AuC of cOFF mice similar to germline *Fmr1* KO mice and significant improvements in EEG measures in cON mice. EEG studies in individuals with FXS report altered network synchrony, including excessive baseline state gamma power and reduced alpha power (Ethridge et al., 2017). Of interest is the gamma-band power, as it is thought to be associated with changes in the activity of fast-spiking inhibitory interneurons. Reduction of PV expression causes GABAergic dysfunction, particularly at gamma frequencies (Lucas et al., 2010), and cortical gamma oscillations are linked to the function of PV interneurons (Cardin et al., 2009; Carlén et al., 2012; Gonzalez-Burgos and Lewis, 2008; Keeley et al., 2017; Sohal et al., 2009; Volman et al., 2011; Guyon et al., 2021). Ray and Maunsell (2011) suggested that the low-gamma band reflects the oscillations that arise through PV neuron firing and synchronization of pyramidal cell activity (Ray and Maunsell, 2011). Similar to germline *Fmr1* KO mice (Lovelace et al., 2018), cOFF mice show reduced gamma synchronization to the chirp stimulus, while the re-expression of FMRP in excitatory neurons during the postnatal P14-P21 period enhanced chirp-elicited phase-locking to 40-55 Hz oscillations and consistently elicited fast gamma range (30-80 Hz) sound-evoked oscillations in adult mice. Our previous study showed that embryonic deletion of *Fmr1* from the forebrain excitatory did not elicit changes in phase-locking to the chirp stimuli (Lovelace et al., 2020). This finding could indicate that *Fmr1* expression in subcortical excitatory neurons might be needed for normal phase locking response to auditory stimuli. Furthermore, our previous study in forebrain excitatory neuron-specific *Fmr1* KO mice also showed that

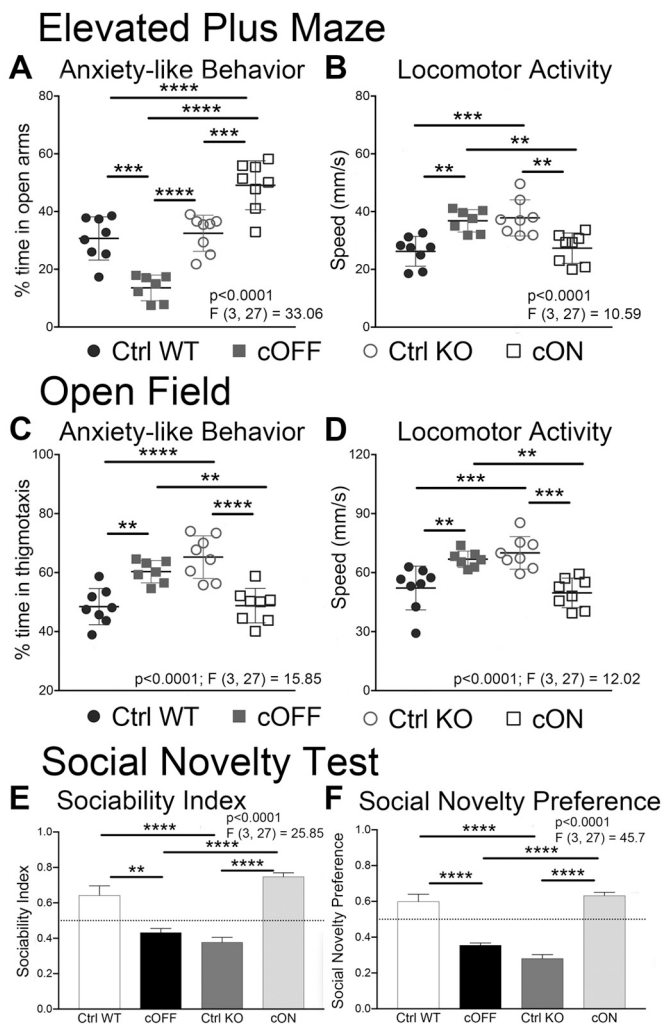

Fig. 8. Postnatal deletion and re-expression of *Fmr1* in excitatory neurons affect behavioral responses in cOFF and cON mice.
(A, B) Graphs demonstrate the performance of Ctrl WT (n = 8), cOFF (n = 7), Ctrl KO (n = 8), and cON (n = 8) in the elevated plus-maze as measured by the percent time in open arms (A) and speed (B). Graphs show mean ± SEM (one-way ANOVA, percent time in open arms: F (3, 27) = 33.06, $p < 0.0001$ and speed: F (3, 27) = 10.59, p < 0.0001 followed by Tukey's multiple comparison post-test **$p < 0.01$, ***$p < 0.001$, ****p < 0.0001; Supplementary Table 6). (C, D) Graphs demonstrate the performance of Ctrl WT (n = 8), cOFF (n = 7), Ctrl KO (n = 8), and cON (n = 8) mice in the open field as measured by the percent time in thigmotaxis (C) and speed (D). Graphs show mean ± SEM (one-way ANOVA, percent time in thigmotaxis: F (3, 27) = 15.85, p < 0.0001 and speed: F (3, 27) = 12.02, p < 0.0001, followed by Tukey's multiple comparison post-test **p < 0.01; ***p < 0.001; ****p < 0.0001; Supplementary Table 5). (E, F) Graphs demonstrate the sociability index (E) and social novelty preference index (F) of Ctrl WT (n = 8), cOFF (n = 7), Ctrl KO (n = 8), and cON (n = 8) mice in the three-chamber test. Graphs show mean ± SEM (one-way ANOVA, sociability index: F (3, 27) = 25.85, p < 0.0001 and social novelty preference index: F (3, 27) = 45.7, p < 0.0001 followed by Tukey's multiple comparison post-test **p < 0.01; ****p < 0.0001; Supplementary Table 6). For the sociability index, values <0.5 indicate more time spent in the empty chamber, >0.5 indicate more time spent in the chamber containing Stranger 1, and 0.5 indicates an equal amount of time in both chambers. For the social novelty preference index, values <0.5 indicate more time spent in the chamber containing Stranger 1 or familiar mouse, >0.5 indicate more time spent in the chamber containing Stranger 2 or new stranger mouse, and 0.5 indicates an equal amount of time in both chambers.

there was a reduction in ITPC in the ~20–30 Hz range immediately after the sound presentation (Lovelace et al., 2020), which was not present in the cOFF mice when *Fmr1* was deleted from excitatory neurons during the postnatal P14-P21 period. Because the auditory system consists of several feed-forward and feedback loops, we cannot discount the potential for nonlinear interactions in terms of cortical deficits influencing sub-cortical processing. Most significant finding is that the re-expression of FMRP suppressed the power of both onset and on-going sound-evoked responses that are abnormally high in *Fmr1* KO mice, indicating the future potential of spatiotemporally targeted reactivation strategies. Gamma band activity is involved in a broad array of sensory and cognitive processes, several of which are affected in FXS. The deficits in gamma phase-locking to sound may cause sensory discrimination deficits (Cardin et al., 2009; Sohal et al., 2009) that may lead to delayed language and cognitive development in FXS. Together, our data suggest that alterations in the development of PV cells driven by FMRP loss in excitatory cells contribute to changes in physiological responses observed in AuC of *Fmr1* KO mice.

Consistent with the role of BDNF-TrkB signaling in the development and function of GABAergic neurons (Berghuis et al., 2006; Nakahara et al., 2004), we observed significant changes in TrkB phosphorylation, which positively correlated with PV expression, suggesting a role of TrkB signaling in regulating PV cells in AuC. TrkB signaling supports PV cells and influences gamma-band synchronization in the hippocampus (Lucas et al., 2014; Zheng et al., 2011). In the cortex, TrkB deletion from PV interneurons resulted in dysregulation of patterned high-frequency cortical activity and disinhibition of local excitatory neurons (Xenos et al., 2018). In *Fmr1* KO mice, BDNF-TrkB signaling was also implicated in FXS-associated alterations (Castren and Castren, 2014) and delayed development of fast-spiking interneurons in the somatosensory cortex (Nomura et al., 2017). Interestingly, hyperactivity and deficits in startle responses were ameliorated in BDNF(+/−)/*Fmr1* KO mice, suggesting a possible role of BDNF/TrkB signaling in these behaviors (Uutela et al., 2012).

Increased anxiety, locomotor activity, and reduced socialization are among the most consistent behavioral symptoms in individuals with FXS (Tranfaglia, 2011). Our studies show that cOFF mice exhibit increased anxiety-like behaviors and locomotor activity and reduced socialization. Conversely, cON mice display reduced anxiety-like behaviors and locomotor activity and increased socialization. Since we didn't see any changes in anxiety-like behaviors when *Fmr1* was embryonically deleted only from forebrain excitatory neurons (Lovelace et al., 2020), this could indicate that the anxiety-like behaviors observed in the cOFF mice are not driven by the absence of *Fmr1* in the forebrain. As several brain areas are involved in these behaviors, including brainstem and basal ganglia, impairments in PV cell development following FMRP deletion from excitatory neurons in subcortical areas may contribute to these abnormal behaviors observed in cOFF mice. Most importantly, re-expression of FMRP in excitatory neurons during postnatal development is sufficient to ameliorate behavior deficits in cON mice, suggesting a potential time window for re-activation studies to improve these behaviors in mice. There are of course several limitations in interpreting the changes in mouse behaviors in terms of translational benefits. In future study, it will be particularly important to assess the translationally relevant EEG phenotypes in mice performing specific behavior tasks that can be also evaluated in humans, such as auditory hypersensitivity test (Ethridge et al., 2017).

In conclusion, our findings show that (1) FMRP loss in excitatory neurons during the period of PV cell maturation affects PV functions leading to various FXS-associated phenotypes; and (2) *Fmr1* re-expression in excitatory neurons during the same period is sufficient for the development of normal cortical responses and improving mouse behaviors. Our understanding of the time period during which these deficits manifest may allow for the development of therapeutic approaches that can potentially be targeted to impact specific cell types, circuits, and symptoms.

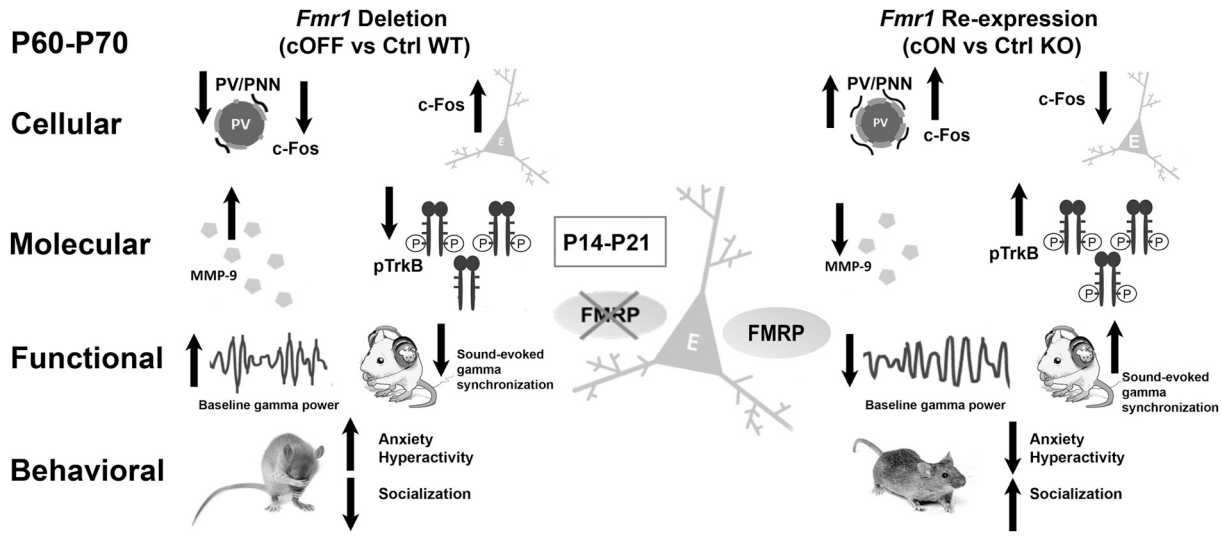

Fig. 9. Schematic of phenotypes observed in adult (P60-P70) mice following deletion or re-expression of *Fmr1* in excitatory neurons during the P14-P21 developmental period. The left panel depicts cellular, molecular, functional, and behavioral phenotypes in adult (P60-P70) mice caused by the cell-specific deletion of *Fmr1* from excitatory neurons during the P14-P28 developmental period. Adult cOFF mice exhibit reduced PV levels and TrkB phosphorylation levels, impaired formation of WFA+ PNNs around PV cells, lower levels of cFOS in PV cells, but upregulated overall cFOS immunoreactivity at baseline, increased gelatinase activity, enhanced baseline gamma power, abnormal chirp-evoked gamma synchronization, and behavioral deficits compared to Ctrl WT mice.
The right panel depicts cellular, molecular, functional, and behavioral phenotypes caused by the cell-specific re-expression of *Fmr1* in cortical excitatory neurons during the P14-P28 period. Adult cON mice exhibit increased PV and TrkB phosphorylation levels, increased WFA+ PNNs around PV cells, higher levels of cFOS in PV cells, but reduced overall cFOS immunoreactivity at baseline, decreased gelatinase activity, normalized neural oscillations, and improved behaviors compared to Ctrl KO mice.

Funding

This work was supported by the National Institute of Child Health and Human Development and the National Institute of Mental Health (1U54 HD082008 to K.A.R. and I.M.E.), U.S. Army Medical Research and Materiel Command (W81XWH-15-1-0436 and W81XWH-15-1-0434 to I.M.E. and K.A.R.), the National Institute of Health and the National Institute of Neurological Disorders and Stroke National Research Service Award Fellowship (1F31NS117178 to M.R), FRAXA Research Foundation Postdoctoral Fellowship to P.S.P. and J.W.L., and University of California President's Postdoctoral Fellowship to P.S.P.

Data availability

All data associated with this study are present in the paper or Supplementary Materials.

Declaration of Competing Interest

The authors report no competing interests

Acknowledgments

The authors thank Dr. Jeffrey Rumschlag, Jamiela Kokash, and Stephen Brookshire for technical support; members of the Ethell, Binder, Goel, and Razak laboratories for helpful discussions; and Dr. David Carter for advice on confocal microscopy.

Appendix A. Supplementary data

Supplementary data to this article can be found online at https://doi.org/10.1016/j.nbd.2021.105577.

References

Anderson, L.A., et al., 2009. Mouse auditory cortex differs from visual and somatosensory cortices in the laminar distribution of cytochrome oxidase and acetylcholinesterase. Brain Res. 1252, 130–142.
Artieda, J., et al., 2004. Potentials evoked by chirp-modulated tones: a new technique to evaluate oscillatory activity in the auditory pathway. Clin. Neurophysiol. 115, 699–709.
Balakrishnan, S., Pearce, R.A., 2014. Spatiotemporal characteristics and pharmacological modulation of multiple gamma oscillations in the CA1 region of the hippocampus. Front. Neural Circuits 8, 150.
Balmer, T.S., 2016. Perineuronal nets enhance the excitability of fast-spiking neurons. eNeuro. 3.
Berghuis, P., et al., 2006. Brain-derived neurotrophic factor selectively regulates dendritogenesis of parvalbumin-containing interneurons in the main olfactory bulb through the PLCgamma pathway. J. Neurobiol. 66, 1437–1451.
Braat, S., Kooy, R.F., 2015. The GABAA receptor as a therapeutic target for neurodevelopmental disorders. Neuron. 86, 1119–1130.
Burgin, K.E., et al., 1990. In situ hybridization histochemistry of Ca2+/calmodulin-dependent protein kinase in developing rat brain. J. Neurosci. 10, 1788–1798.
Cabungcal, J.H., et al., 2013. Perineuronal nets protect fast-spiking interneurons against oxidative stress. Proc. Natl. Acad. Sci. U. S. A. 110, 9130–9135.
Cardin, J.A., et al., 2009. Driving fast-spiking cells induces gamma rhythm and controls sensory responses. Nature. 459, 663–667.
Carlén, M., et al., 2012. A critical role for NMDA receptors in parvalbumin interneurons for gamma rhythm induction and behavior. Mol. Psychiatry 17, 537–548.
Castren, M.L., Castren, E., 2014. BDNF in fragile X syndrome. Neuropharmacology 76 (Pt C), 729–736.
Castrén, M., et al., 2003. Augmentation of auditory N1 in children with fragile X syndrome. Brain Topogr. 15, 165–171.
Chen, L., Toth, M., 2001. Fragile X mice develop sensory hyperreactivity to auditory stimuli. Neuroscience. 103, 1043–1050.
Chen, G., et al., 2017. Distinct inhibitory circuits orchestrate cortical beta and gamma band oscillations. Neuron. 96 (1403–1418), e6.
Chittajallu, R., Isaac, J.T., 2010. Emergence of cortical inhibition by coordinated sensory-driven plasticity at distinct synaptic loci. Nat. Neurosci. 13, 1240–1248.
Contractor, A., et al., 2015. Altered neuronal and circuit excitability in fragile X syndrome. Neuron. 87, 699–715.
Contractor, A., et al., 2021. Cortical interneurons in autism. Nat. Neurosci. 24, 1648–1659.
Crawford, D.C., et al., 2001. FMR1 and the fragile X syndrome: human genome epidemiology review. Genet Med. 3, 359–371.
Daw, M.I., et al., 2007. Coordinated developmental recruitment of latent fast spiking interneurons in layer IV barrel cortex. Nat. Neurosci. 10, 453–461.
Denaxa, M., et al., 2018. Modulation of apoptosis controls inhibitory interneuron number in the cortex. Cell Rep. 22, 1710–1721.

Dorrn, A.L., et al., 2010. Developmental sensory experience balances cortical excitation and inhibition. Nature. 465, 932–936.
Dvorak, D., Fenton, A.A., 2014. Toward a proper estimation of phase-amplitude coupling in neural oscillations. J. Neurosci. Methods 225, 42–56.
Ethridge, L.E., et al., 2016. Reduced habituation of auditory evoked potentials indicate cortical hyper-excitability in fragile X syndrome. Transl. Psychiatry 6, e787.
Ethridge, L.E., et al., 2017. Neural synchronization deficits linked to cortical hyper-excitability and auditory hypersensitivity in fragile X syndrome. Mol. Autism. 8, 22.
Ferguson, B.R., Gao, W.J., 2018. PV interneurons: critical regulators of E/I balance for prefrontal cortex-dependent behavior and psychiatric disorders. Front. Neural Circuits 12, 37.
Filice, F., et al., 2020. The Parvalbumin hypothesis of autism Spectrum disorder. Front. Cell. Neurosci. 14, 577525.
Frankland, P.W., et al., 2004. Sensorimotor gating abnormalities in young males with fragile X syndrome and Fmr1-knockout mice. Mol. Psychiatry 9, 417–425.
Fu, Y., et al., 2015. A cortical disinhibitory circuit for enhancing adult plasticity. Elife. 4, e05558.
Gatto, C.L., Broadie, K., 2008. Temporal requirements of the fragile X mental retardation protein in the regulation of synaptic structure. Development. 135, 2637–2648.
Gibson, J.R., et al., 2008. Imbalance of neocortical excitation and inhibition and altered UP states reflect network hyperexcitability in the mouse model of fragile X syndrome. J. Neurophysiol. 100, 2615–2626.
Goel, A., et al., 2018. Impaired perceptual learning in a mouse model of fragile X syndrome is mediated by parvalbumin neuron dysfunction and is reversible. Nat. Neurosci. 21, 1404–1411.
Gonzalez-Burgos, G., Lewis, D.A., 2008. GABA neurons and the mechanisms of network oscillations: implications for understanding cortical dysfunction in schizophrenia. Schizophr. Bull. 34, 944–961.
Guyon, N., et al., 2021. Network asynchrony underlying increased broadband gamma power. J. Neurosci. 41, 2944–2963.
Hampson, D.R., et al., 2019. The application of adeno-associated viral vector gene therapy to the treatment of Fragile X syndrome. Brain Sci. 9.
Han, Y.K., et al., 2007. Early experience impairs perceptual discrimination. Nat. Neurosci. 10, 1191.
Harkness, J.H., et al., 2019. Sleep disruption elevates oxidative stress in parvalbumin-positive cells of the rat cerebral cortex. Sleep. 42.
Hashemi, E., et al., 2017. The number of Parvalbumin-expressing interneurons is decreased in the prefrontal cortex in autism. Cereb. Cortex 27, 1931–1943.
Hays, S.A., et al., 2011. Altered neocortical rhythmic activity states in Fmr1 KO mice are due to enhanced mGluR5 signaling and involve changes in excitatory circuitry. J. Neurosci. 31, 14223–14234.
Hu, H., et al., 2014. Interneurons. Fast-spiking, parvalbumin(+) GABAergic interneurons: from cellular design to microcircuit function. Science 345, 1255263.
Hussman, J.P., 2001. Suppressed GABAergic inhibition as a common factor in suspected etiologies of autism. J. Autism Dev. Disord. 31, 247–248.
Insanally, M.N., et al., 2009. Feature-dependent sensitive periods in the development of complex sound representation. J. Neurosci. 29, 5456–5462.
Kawaguchi, Y., et al., 1987. Fast spiking cells in rat hippocampus (CA1 region) contain the calcium-binding protein parvalbumin. Brain Res. 416, 369–374.
Keeley, S., et al., 2017. Modeling fast and slow gamma oscillations with interneurons of different subtype. J. Neurophysiol. 117, 950–965.
Kim, H., et al., 2013. Impaired critical period plasticity in primary auditory cortex of fragile X model mice. J. Neurosci. 33, 15686–15692.
Koeppen, J., et al., 2018. Functional consequences of synapse Remodeling following astrocyte-specific regulation of Ephrin-B1 in the adult hippocampus. J. Neurosci. 38, 5710–5726.
Kulinich, A.O., et al., 2020. Beneficial effects of sound exposure on auditory cortex development in a mouse model of fragile X syndrome. Neurobiol. Dis. 134, 104622.
LeBlanc, J.J., Fagiolini, M., 2011. Autism: a "critical period" disorder? Neural Plast. 2011, 921680.
Lee, E., et al., 2017. Excitation/inhibition imbalance in animal models of autism Spectrum disorders. Biol. Psychiatry 81, 838–847.
Lensjø, K.K., et al., 2017. Removal of Perineuronal nets unlocks juvenile plasticity through network mechanisms of decreased inhibition and increased gamma activity. J. Neurosci. 37, 1269–1283.
Lim, L., et al., 2018. Development and functional diversification of cortical interneurons. Neuron. 100, 294–313.
Lovelace, J.W., et al., 2016. Matrix metalloproteinase-9 deletion rescues auditory evoked potential habituation deficit in a mouse model of fragile X syndrome. Neurobiol. Dis. 89, 126–135.
Lovelace, J.W., et al., 2018. Translation-relevant EEG phenotypes in a mouse model of fragile X syndrome. Neurobiol. Dis. 115, 39–48.
Lovelace, J.W., et al., 2020. Deletion of Fmr1 from forebrain excitatory neurons triggers abnormal cellular, EEG, and Behavioral phenotypes in the auditory cortex of a mouse model of fragile X syndrome. Cereb. Cortex 30, 969–988.
Lucas, E.K., et al., 2010. Parvalbumin deficiency and GABAergic dysfunction in mice lacking PGC-1alpha. J. Neurosci. 30, 7227–7235.
Lucas, E.K., et al., 2014. Mice lacking TrkB in parvalbumin-positive cells exhibit sexually dimorphic behavioral phenotypes. Behav. Brain Res. 274, 219–225.
Lunden, J.W., et al., 2019. Cortical interneuron function in autism spectrum condition. Pediatr. Res. 85, 146–154.
Marin, O., 2012. Interneuron dysfunction in psychiatric disorders. Nat. Rev. Neurosci. 13, 107–120.
Marin, O., 2016. Developmental timing and critical windows for the treatment of psychiatric disorders. Nat. Med. 22, 1229–1238.
Maris, E., Oostenveld, R., 2007. Nonparametric statistical testing of EEG- and MEG-data. J. Neurosci. Methods 164, 177–190.
Martin del Campo, H.N., et al., 2012. Parvalbumin immunoreactivity in the auditory cortex of a mouse model of presbycusis. Hear. Res. 294, 31–39.
Mientjes, E.J., et al., 2006. The generation of a conditional Fmr1 knock out mouse model to study Fmrp function in vivo. Neurobiol. Dis. 21, 549–555.
Miller, L.J., et al., 1999. Electrodermal responses to sensory stimuli in individuals with fragile X syndrome: a preliminary report. Am. J. Med. Genet. 83, 268–279.
Nakahara, H., et al., 2004. Specialization of primary auditory cortex processing by sound exposure in the "critical period". Proc. Natl. Acad. Sci. U. S. A. 101, 7170–7174.
Nguyen, A.Q., et al., 2020. Astrocytic Ephrin-B1 controls excitatory-inhibitory balance in developing hippocampus. J. Neurosci. 40, 6854–6871.
Niell, C.M., Stryker, M.P., 2010. Modulation of visual responses by behavioral state in mouse visual cortex. Neuron. 65, 472–479.
Nielsen, D.M., et al., 2002. Alterations in the auditory startle response in Fmr1 targeted mutant mouse models of fragile X syndrome. Brain Res. 927, 8–17.
Nikolakopoulou, A.M., et al., 2016. Astrocytic Ephrin-B1 regulates synapse remodeling following traumatic brain injury. ASN Neuro 8, 1–18.
Nomura, T., et al., 2017. Delayed maturation of fast-spiking interneurons is rectified by activation of the TrkB receptor in the mouse model of fragile X syndrome. J. Neurosci. 37, 11298–11310.
Nygaard, K.R., et al., 2019. Erroneous inference based on a lack of preference within one group: autism, mice, and the social approach task. Autism Res. 12, 1171–1183.
Okray, Z., et al., 2015. A novel fragile X syndrome mutation reveals a conserved role for the carboxy-terminus in FMRP localization and function. EMBO Mol. Med. 7, 423–437.
Orefice, L.L., Zimmerman, A.L., Chirila, A.M., Sleboda, S.J., Head, J.P., Ginty, D.D., 2016. Peripheral mechanosensory neuron dysfunction underlies tactile and behavioral deficits in mouse models of ASDs. Cell. 166, 299–313.
Paxinos, G., Franklin, K.B., 2004. The Mouse Brain in Stereotaxic Coordinates. Gulf professional publishing.
Penagarikano, O., et al., 2007. The pathophysiology of fragile x syndrome. Annu. Rev. Genomics Hum. Genet. 8, 109–129.
Pérez-Alcázar, M., et al., 2008. Chirp-evoked potentials in the awake and anesthetized rat. A procedure to assess changes in cortical oscillatory activity. Exp. Neurol. 210, 144–153.
Pirbhoy, P.S., et al., 2020. Acute pharmacological inhibition of matrix metalloproteinase-9 activity during development restores perineuronal net formation and normalizes auditory processing in Fmr1 KO mice. J. Neurochem. 155, 538–558.
Pizzorusso, T., et al., 2002. Reactivation of ocular dominance plasticity in the adult visual cortex. Science. 298, 1248–1251.
Popescu, M.V., Polley, D.B., 2010. Monaural deprivation disrupts development of binaural selectivity in auditory midbrain and cortex. Neuron. 65, 718–731.
Purcell, D.W., et al., 2004. Human temporal auditory acuity as assessed by envelope following responses. J. Acoust. Soc. Am. 116, 3581–3593.
Rais, M., et al., 2018. Sensory processing phenotypes in fragile X syndrome. ASN Neuro. 10, 1759091418801092.
Ray, S., Maunsell, J.H., 2011. Different origins of gamma rhythm and high-gamma activity in macaque visual cortex. PLoS Biol. 9, e1000610.
Reinhard, S.M., et al., 2019. Reduced perineuronal net expression in Fmr1 KO mice auditory cortex and amygdala is linked to impaired fear-associated memory. Neurobiol. Learn. Mem. 164, 107042.
del Rio, J.A., et al., 1994. The development of parvalbumin-immunoreactivity in the neocortex of the mouse. Brain Res. Dev. Brain Res. 81, 247–259.
Rojas, D.C., et al., 2001. Auditory evoked magnetic fields in adults with fragile X syndrome. Neuroreport. 12, 2573–2576.
Rossignol, E., 2011. Genetics and function of neocortical GABAergic interneurons in neurodevelopmental disorders. Neural Plast. 2011, 649325.
Rotschafer, S., Razak, K., 2013. Altered auditory processing in a mouse model of fragile X syndrome. Brain Res. 1506, 12–24.
Rotschafer, S.E., Razak, K.A., 2014. Auditory processing in fragile x syndrome. Front. Cell. Neurosci. 8, 19.
Rubenstein, J.L., Merzenich, M.M., 2003. Model of autism: increased ratio of excitation/inhibition in key neural systems. Genes Brain Behav. 2, 255–267.
Schneider, A., et al., 2013. Electrocortical changes associated with minocycline treatment in fragile X syndrome. J. Psychopharmacol. 27, 956–963.
Selby, L., et al., 2007. Major defects in neocortical GABAergic inhibitory circuits in mice lacking the fragile X mental retardation protein. Neurosci. Lett. 412, 227–232.
Shitik, E.M., et al., 2020. Reactivation of FMR1 gene expression is a promising strategy for fragile X syndrome therapy. Gene Ther. 27, 247–253.
Sidhu, H., et al., 2014. Genetic removal of matrix metalloproteinase 9 rescues the symptoms of fragile X syndrome in a mouse model. J. Neurosci. 34, 9867–9879.
Siegel, J.J., et al., 2017. Prefrontal cortex dysfunction in fragile X mice depends on the continued absence of fragile X mental retardation protein in the adult brain. J. Neurosci. 37, 7305–7317.
Sinclair, D., et al., 2017. Sensory processing in autism spectrum disorders and fragile X syndrome-from the clinic to animal models. Neurosci. Biobehav. Rev. 76, 235–253.
Slaker, M., et al., 2016a. Impact of environmental enrichment on Perineuronal nets in the prefrontal cortex following early and late abstinence from sucrose self-Administration in Rats. PLoS One 11, e0168256.
Slaker, M., et al., 2016b. Caught in the net: Perineuronal nets and addiction. Neural Plast. 2016, 7538208.
Slaker, M.L., et al., 2016c. A standardized and automated method of perineuronal net analysis using. IBRO Rep. 1, 54–60.
Sohal, V.S., et al., 2009. Parvalbumin neurons and gamma rhythms enhance cortical circuit performance. Nature. 459, 698–702.

Southwell, D.G., et al., 2012. Intrinsically determined cell death of developing cortical interneurons. Nature. 491, 109–113.
Sun, Y.J., et al., 2010. Fine-tuning of pre-balanced excitation and inhibition during auditory cortical development. Nature 465, 927–931.
Sutcliffe, J.S., et al., 1992. DNA methylation represses FMR-1 transcription in fragile X syndrome. Hum. Mol. Genet. 1, 397–400.
Tabolacci, E., et al., 2016. Transcriptional reactivation of the FMR1 gene. A possible approach to the treatment of the Fragile X syndrome. Genes (Basel) 7.
Tallon-Baudry, C., et al., 1996. Stimulus specificity of phase-locked and non-phase-locked 40 Hz visual responses in human. J. Neurosci. 16, 4240–4249.
Tamamaki, N., et al., 2003. Green fluorescent protein expression and colocalization with calretinin, parvalbumin, and somatostatin in the GAD67-GFP knock-in mouse. J. Comp. Neurol. 467, 60–79.
Tranfaglia, M.R., 2011. The psychiatric presentation of fragile x: evolution of the diagnosis and treatment of the psychiatric comorbidities of fragile X syndrome. Dev. Neurosci. 33, 337–348.
Uutela, M., et al., 2012. Reduction of BDNF expression in Fmr1 knockout mice worsens cognitive deficits but improves hyperactivity and sensorimotor deficits. Genes Brain Behav. 11, 513–523.
Verkerk, A.J., et al., 1991. Identification of a gene (FMR-1) containing a CGG repeat coincident with a breakpoint cluster region exhibiting length variation in fragile X syndrome. Cell. 65, 905–914.
Vershkov, D., et al., 2019. FMR1 reactivating treatments in fragile X iPSC-derived neural progenitors in vitro and in vivo. Cell Rep. 26 (2531–2539), e4.
de Villers-Sidani, E., et al., 2007. Critical period window for spectral tuning defined in the primary auditory cortex (A1) in the rat. J. Neurosci. 27, 180–189.
Volman, V., et al., 2011. Downregulation of parvalbumin at cortical GABA synapses reduces network gamma oscillatory activity. J. Neurosci. 31, 18137–18148.
Wang, X., et al., 2013. Distribution of CaMKIIalpha expression in the brain in vivo, studied by CaMKIIalpha-GFP mice. Brain Res. 1518, 9–25.
Wen, T.H., et al., 2018. Genetic reduction of matrix Metalloproteinase-9 promotes formation of Perineuronal nets around Parvalbumin-expressing interneurons and normalizes auditory cortex responses in developing Fmr1 Knock-out mice. Cereb. Cortex 28, 3951–3964.
Wong, F.K., et al., 2018. Pyramidal cell regulation of interneuron survival sculpts cortical networks. Nature. 557, 668–673.
Xenos, D., et al., 2018. Loss of TrkB Signaling in Parvalbumin-expressing basket cells results in network activity disruption and abnormal behavior. Cereb. Cortex 28, 3399–3413.
Zhang, L.I., et al., 2001. Persistent and specific influences of early acoustic environments on primary auditory cortex. Nat. Neurosci. 4, 1123–1130.
Zheng, K., et al., 2011. TrkB signaling in parvalbumin-positive interneurons is critical for gamma-band network synchronization in hippocampus. Proc. Natl. Acad. Sci. U. S. A. 108, 17201–17206.